

Coherent nonlinear optical probe for cavity-dressed vibrational mode mixing: multidimensional double-quantum coherence and photon-echo signal

Arunangshu Debnath^{1,*}

¹*Theory Division, Center for Free-Electron Laser Science CFEL,
Deutsches Elektronen-Synchrotron DESY, Notkestrasse 85, 22607 Hamburg, Germany*

Cavity modulation of interacting molecular vibrational modes promises an expanded role of the characteristic vibrations to act as spectroscopic markers. In addition to the intrinsic, inter-mode and extrinsic, cavity-mediated inter-mode delocalization, the vibrational modes undergo multiscale relaxation due to reservoir vibrations. Two complementary coherent multidimensional spectroscopic techniques are presented, which reveal the dynamical nature of the mode correlations in the presence relaxation. Simulations are presented for finite laser pulses. The chosen cavity-vibron mode coupling strengths fall within the range of inter-vibrational mode coupling, hinting at a parameter regime where vibrational energy dispersal can be controlled. It is highlighted that the cavity manipulation of vibrational double excitations, namely, overtone and combination states, can offer deeper insights into the collective mode dynamics. These observations set the ground for cavity-controlled spectroscopic investigation of mode-selective dynamics, where localized electromagnetic modes function as an effective few-body coupler of vibrations.

I. INTRODUCTION

Spectrally distinct vibrational modes, prevalent in molecular systems, often serve as spectroscopic markers for monitoring the underlying material dynamics. These vibrational modes, with characteristic spectral-temporal properties, are traditionally manipulated via external optical fields in the IR regime. [1–11]. However, such frequency-to-mode assignment workflow gets even more challenging in the presence of surrounding vibrations that acts as a source of spectral broadening and spectral weight redistribution. Ultrafast mode correlation dynamics of the vibrational modes can be systematically investigated by multiple, temporally controlled, coherent laser-matter interactions. Previous experiments have demonstrated the usage of externally tunable laser fields to explore the physical processes such as solvation [12–14], chemical transformation [15–17], conformational changes of proteins, and peptides [18, 19]. These spectroscopic techniques, collectively referred to as multidimensional coherent spectroscopy (MDCS) act as a non-linear probe into the vibrational mode dynamics [5, 20–29]. Tailoring of the external optical fields via pulse shaping techniques enables additional control over temporal and spectral properties of matter dynamics and allows the studies to be carried out in a mode-specific manner.

Over recent years, material polarization has been controlled via another tool: localized electromagnetic fields [30–51]. Typically, the mode distributions of these electromagnetic fields can be engineered, and the coupling strengths with localized vibrations can be optimized. Previous investigations on collective vibrational properties interacting with confined electromagnetic fields provide evidence of plausible dynamical and static modifications [42, 52–59]. In addition, previous theoretical and experimental studies have established the usefulness of time-resolved vibrational spectroscopic techniques in investigating such systems [60–67].

Molecular vibrations exhibit spectrally structured, spatially localized mode distributions. In contrast, molecular solvents are characterized by spatially extended, broad spectral distributions, often serving as a spectral background. In comparison, cavity modes, particularly in the “good cavity” regime, exhibit characteristics such as spectrally narrow, and well-defined, yet tunable, spatially extended electromagnetic mode functions. Investigating the ultrafast vibrational spectroscopy of such interacting spectroscopic markers in the presence of external cavities presents an intriguing prospect.

The cavity electromagnetic modes primarily interact with the electronic polarization. These locally modified polarization changes often crucially affect the properties of the vibrations. Frequently, they induce measurable changes in the energy regime of vibrations which affect quantities that are spectroscopically relevant. The vibrational quasiparticle picture which is capable of describing the coherent vibrational dynamics in molecules can offer a viable description for the cavity-dressed picture as well. Throughout this article, the cavity-dressed vibrational modes, in the quasiparticle picture, are referred to as vibron polaritons. The auxiliary molecular vibrations are referred to as phonons.

In this article, I focus on stimulated nonlinear signals that are capable of revealing the vibron-polariton correlation

* arunangshu.debnath@desy.de; arunangshu.episteme99.com

and transport dynamics at the ultrafast timescale. Stimulated signals arise from the energy exchange between respective vibron-polariton modes and the external optical field modes, hence offering capabilities to systematically isolate the explicit cavity mediated effects. Specifically, the dynamics of vibron-polaritons are investigated via multiple, weak-field laser-matter interactions, under the assumption that the cavity mode is being pumped by low-intensity, time-dependent optical fields. Two complementary techniques, Photon Echo (PE) and Double Quantum Coherence (DQC), are numerically simulated to explore the cavity-mediated correlated vibrational mode dynamics in the presence of phonon dissipation. In Section II, the model of interacting multimode vibrational dynamics, which are

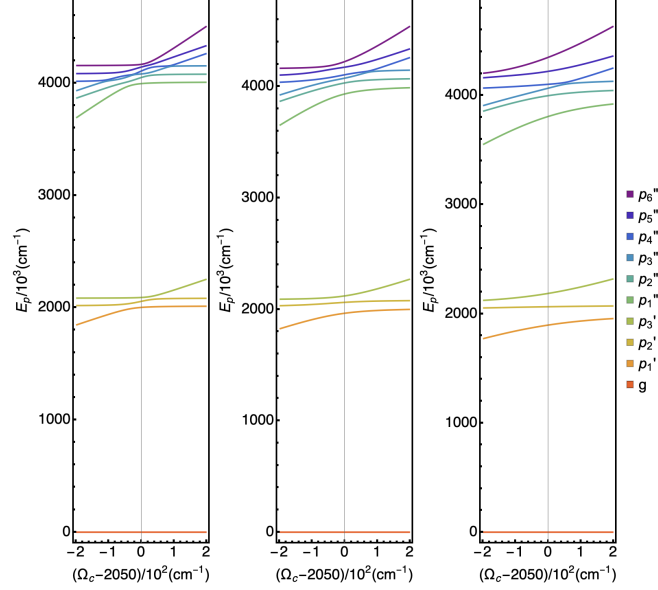


FIG. 1: The panel displays the parametric energy levels of one-polariton and two-polariton states as a function of cavity mode frequency, for three distinct coupling strengths. As expected, increased state repulsion is observed at higher coupling strengths. Resonant laser driving promotes transitions between the branches and enable selective probing of specific vibron-polariton resonances.

simultaneously coupled to a cavity mode and phonon reservoir, is introduced, and the laser-polariton interactions are defined. Furthermore, the nature of the one- and two-vibron-polariton states is analyzed, and the corresponding Green's functions are defined. The latter will be utilized in the evaluation of the optical signals. In Section III, the expressions for the aforementioned multidimensional coherent spectroscopy (MDCS) techniques are presented, along with numerical simulations. The insights that these numerical simulations offer into ultrafast vibron-polariton kinetics are also discussed. In Section IV, a concluding discussion is presented, where the benefits of the parameter regime are highlighted, the limitations are emphasized, and ongoing efforts are outlined.

II. DISSIPATIVE ONE- AND TWO-POLARITON KINETICS

A. Hamiltonian

A multimode, quasi-particle based description of the interacting vibron-cavity-phonon system can be derived from the ab initio Hamiltonian A. The corresponding Hamiltonian can be presented as:

$$\begin{aligned}
 H_p = & \sum_{mn} (E_m \delta_{mn} + J_{mn}) B_m^\dagger B_n + U_{mn}^{(2)} B_m^\dagger B_n^\dagger B_m B_n \\
 & + \sum_m \sum_{k_c} \omega_{k_c}^{(c)} a_{k_c}^\dagger a_{k_c} + \sum_{m, k_c} g_{mk_c}^{(c)} (a_{k_c}^\dagger B_m + B_m^\dagger a_{k_c}) \\
 & + \sum_m \sum_k \omega_k^{(b)} b_k^\dagger b_k + \sum_{m, k} g_{mk}^{(b)} B_m^\dagger B_m (b_k + b_k^\dagger)
 \end{aligned} \tag{1}$$

In the above, the first two terms represent interacting, local vibron modes with onsite excitation energy E_m , inter-mode coupling energy J_{mn} , and quartic nonlinearity parameter, $U_{mn}^{(2)}$. The magnitude of inter-mode coupling parameters can be estimated from the nature of transition dipole matrix elements, inter-mode distances and relative orientations. The mode nonlinearity parameters, for $m = n$ and $m \neq n$, depend on the nature of the static dipole matrix elements and affect the anharmonicity of vibron modes. Together, they govern the extent of delocalization of the vibron states in the real space in the absence of cavity. The vibron creation (annihilation) operators, $B_m^\dagger (B_m)$ follow the commutations relations $[B_m^\dagger, B_n] = \delta_{mn}$ and $[B_m, B_n] = [B_m^\dagger, B_n^\dagger] = 0$. Cooperative vibrational excitations hosted in cavity-free systems can be classified in terms of the combination and overtones modes. These terms refer to the inter-mode two-vibron and intra-mode two-vibron states, respectively. The corresponding states display distinct spectral features depending on the magnitude of the mode nonlinearity parameters $U_{mn}^{(2)}$.

The vibron modes interact with the external collective vibrations, hereafter termed as phonons, characterized by the coupling strengths $g_{mk}^{(b)}$ to the vibron modes. The corresponding Hamiltonian terms are represented by the fifth and the sixth term in Eq. 1. The phonon mode creation (annihilation) operators $b_k^\dagger (b_k)$, with respective frequencies $\omega_k^{(b)}$, follow the free-boson commutation relations, $[b_j, b_{j'}] = [b_j^\dagger, b_{j'}^\dagger] = 0$ and $[b_j, b_{j'}^\dagger] = \delta_{jj'}$. The noninteracting phonon modes are often described by the distribution of the coupling strengths in the continuum limit. These phonon modes may describe molecular solvent or surrounding vibrational fluctuations in different scenarios.

The third and the fourth Hamiltonian term represents the cavity and cavity-vibron mode coupling Hamiltonian, respectively. The cavity-vibron mode coupling, governed by tunable parameters $g_{mk_c}^{(c)}$, create further delocalization of the states that extends over both the vibron and cavity modes. In this work, the bare cavity frequency is treated in the idealized limit of a narrowband, cavity mode having a low decay rate, given by, $\omega_{k_c}^{(c)}$. The number of cavity modes have been restricted to $k_c = 1$, with occupations extended to include two-quantum cavity transitions. It is noted that the cavity mode energy, ω_c exhibit dependence on the angle of incidence of the laser sources, θ , and the dielectric properties of the filled media, n_{ind} , as given by $\omega_c = \omega_0 / (\sqrt{1 - \sin^2 \theta / n_{\text{ind}}^2})$. The semi-empirical coupling, for Distributed Bragg Reflector (DBR) Fabry-Perot cavity types, where two layers encapsulate the sample region, is influenced by the cavity volume $V = \lambda / n_{\text{ind}}$ (where λ represents the resonant cavity wavelength and n_{ind} is the effective intra-cavity refractive index). This volume determines the coupling strengths via $g_{mk_c}^{(c)} = \sqrt{N} d_c \cdot E_c \sqrt{\omega_c / 2\epsilon_0 V}$ (where N is the number of molecules interacting with the mode indexed c , $d_c(E_c)$ is the transition dipole moment (electric field vector) of the cavity mode, and V_c is the of the cavity mode volume). Both of these parameters are treated as tunable in this study.

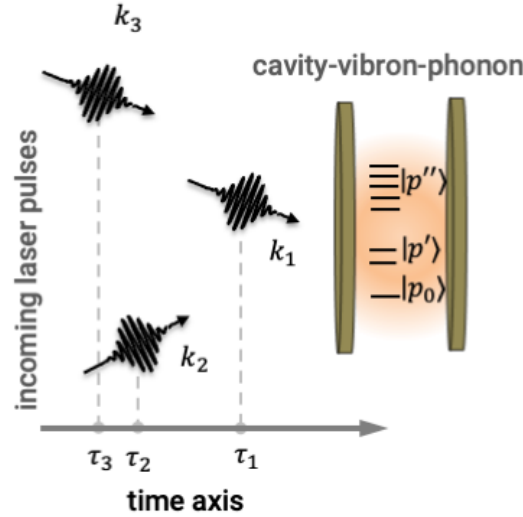


FIG. 2: Schematic diagram illustrating a potential multi-pulse configuration suitable for the acquisition of multidimensional coherent spectroscopic signals. For clarity, relative dimensions within the illustration have been exaggerated. The employed three-band polariton model incorporates the two-polariton process that contributes to the observed polarization.

B. Vibron-cavity tensor-product basis and vibron-polariton states

The energy states and dynamics can be described by expanding the Hamiltonian in the tensor-product basis of vibron-cavity mode configurations, i.e., $|n_{v_2}n_{v_1}n_c\rangle = |n_{v_2}n_{v_1}\rangle|n_c\rangle_c$, where the $n_v(n_c)$ denoted the occupation number of vibron (cavity) modes. The physical processes relevant for the weak-field three-pulse double-quantum coherence and photon-echo signal are restricted to states involving one- and two-quantum excitations. The latter allows the basis set to be truncated for all practical purposes. However, such a truncated basis set accommodates the theoretical description of two-quantum, pure (inter- and intra-mode excitations residing in either vibron or cavity mode), and mixed (inter-mode excitations residing in both vibron and cavity) excitations. Identifying the dynamical role of these excitations at the ultrafast timescale in the presence of phonon interactions remains one of the principal aims of this article.

The vibron-polariton or cavity-dressed vibron eigenstates are determined through the exact diagonalization of the first four terms of the Hamiltonian presented in Eq. (1). The one ($|p'\rangle$) and two ($|p''\rangle$) polariton states are expressed as

$$|p'\rangle = \sum_{mk_c} (\phi_{mp'}^{(1)} B_s^\dagger + \phi_{k_c p'}^{(1)} a_{k_c}^\dagger) |g\rangle \quad (2)$$

$$|p''\rangle = \sum_{mnk_{c,i}k_{c,j}} (\phi_{mnp''}^{(2)} B_m^\dagger B_n^\dagger + \phi_{mk_{c,i}p''}^{(2)} B_m^\dagger a_{k_{c,i}}^\dagger + \phi_{k_{c,i}k_{c,j}p''}^{(2)} a_{k_{c,i}}^\dagger a_{k_{c,j}}^\dagger) |g\rangle \quad (3)$$

In total, $n_0 = 1$ ground state, $n_{p'} = 3$ one-polariton states, and $n_{p''} = 6$ two-polariton are obtained, distributed in three number conserving manifolds. The transformation matrix elements for the respective polariton manifolds, $\phi_{ab}^{(n)}$, encode the necessary information regarding the degree of delocalization of the polariton states across the vibron and cavity modes.

It is important to recall that the exact diagonalization procedure formally incorporates the effects of intermode hopping and cavity-vibron coupling to all orders. The polariton energy levels for the parametric variation of the cavity frequency are presented in Fig. 1, for three values of the coupling strengths. Here, the state of mixing and repulsion within a manifold is a joint function of cavity coupling strengths, the magnitudes of inter-mode hopping, and cavity detuning. The vertical section in any of the plots provides the relative ordering of the energy levels; the corresponding gaps are observed in spectroscopic measurements.

The nature of these polariton states can be better understood by analyzing the vibron-cavity tensor-product basis (see Fig. 3). The one-excitation manifold is spanned by states $|10\rangle|0\rangle_c$, $|01\rangle|0\rangle_c$ and $|00\rangle|1\rangle_c$, where the first two represent pure vibron states, and the last one represents a mixed cavity-vibron state. In the one-excitation subspace, the cavity-vibron interaction term mediates transitions between the states $|01\rangle|0\rangle_c$ and $|10\rangle|0\rangle_c$ through the state $|00\rangle|1\rangle_c$. In the absence of a cavity, such inter-mode excitation transfer can also be influenced by the Coulomb-induced hopping term. Within the framework of the chosen model, the relative propensity of these two processes is governed by the relative magnitudes of J_{mn} and $g_{mk_c}^{(c)}$. These effects are hidden in the state transformation matrix elements, and can be observed by monitoring the polariton state delocalization. The two excitation manifold is spanned by six states, comprising pure two-vibron states ($|20\rangle|0\rangle_c$, $|02\rangle|0\rangle_c$, $|11\rangle|0\rangle_c$), pure two-photon cavity states ($|00\rangle|2\rangle_c$), and mixed cavity-vibron states ($|10\rangle|1\rangle_c$, $|01\rangle|1\rangle_c$). The cavity mode mediates transitions between the pure two-vibron and two-photon cavity subspaces via the mixed cavity-vibron configurations. For example, the cavity-mediated interactions induce transitions between $|20\rangle|0\rangle_c$ and $|02\rangle|0\rangle_c$ via $|10\rangle|1\rangle_c$ and $|01\rangle|1\rangle_c$. The interaction term that includes simultaneous one quantum excitation (de-excitation) involving the cavity and vibron mode facilitates such transition. It is useful to recall that the pure two-vibron subspace contains coulomb interaction mediated intra-mode couplings that result in a relatively complex delocalization across sites.

For the numerical simulation, the energies of the localized vibrational modes are specified as $E_1 = 2019 \text{ cm}^{-1}$ and $E_2 = 2080 \text{ cm}^{-1}$, respectively, while the hopping energy scales are $J_{12} = J_{21} = -16 \text{ cm}^{-1}$. The nonlinearity parameters are $U_{11}^{(2)} = -11 \text{ cm}^{-1}$, $U_{22}^{(2)} = -14 \text{ cm}^{-1}$, and $U_{12}^{(2)} = -14 \text{ cm}^{-1}$. These values influence the overtone and combination two-vibron states even in the absence of cavity interactions. Such energy values are comparable to the energy scales associated with carbonyl stretching vibrations of metal carbonyl complexes, for instance, $\text{Rh}(\text{CO})_2\text{C}_5\text{H}_7\text{O}_2$ in RDC. The cavity mode energy is taken as, $E_c = 2050 \text{ cm}^{-1}$ which couples uniformly to the two vibron modes with coupling strengths specified by $g_{1,k_c}^{(c)} = g_{2,k_c}^{(c)} = 25 \text{ cm}^{-1}$. Notably, the cavity mode is detuned from the resonance energy of both the bare one-vibron modes. Three one-polariton states and six two-polariton states are obtained with energy values (in cm^{-1}) $\{1996.59, 2058.21, 2094.2, \}$ and $\{4011.45, 4030.4, 4088.37, 4111.39, 4149.21, 4165.19\}$. The principal aim of the presented study is to track the dynamics of these states via two complementary spectroscopic techniques in the presence of spectral fluctuation, dephasing, and relaxation. The vibron-phonon coupling strengths for the two

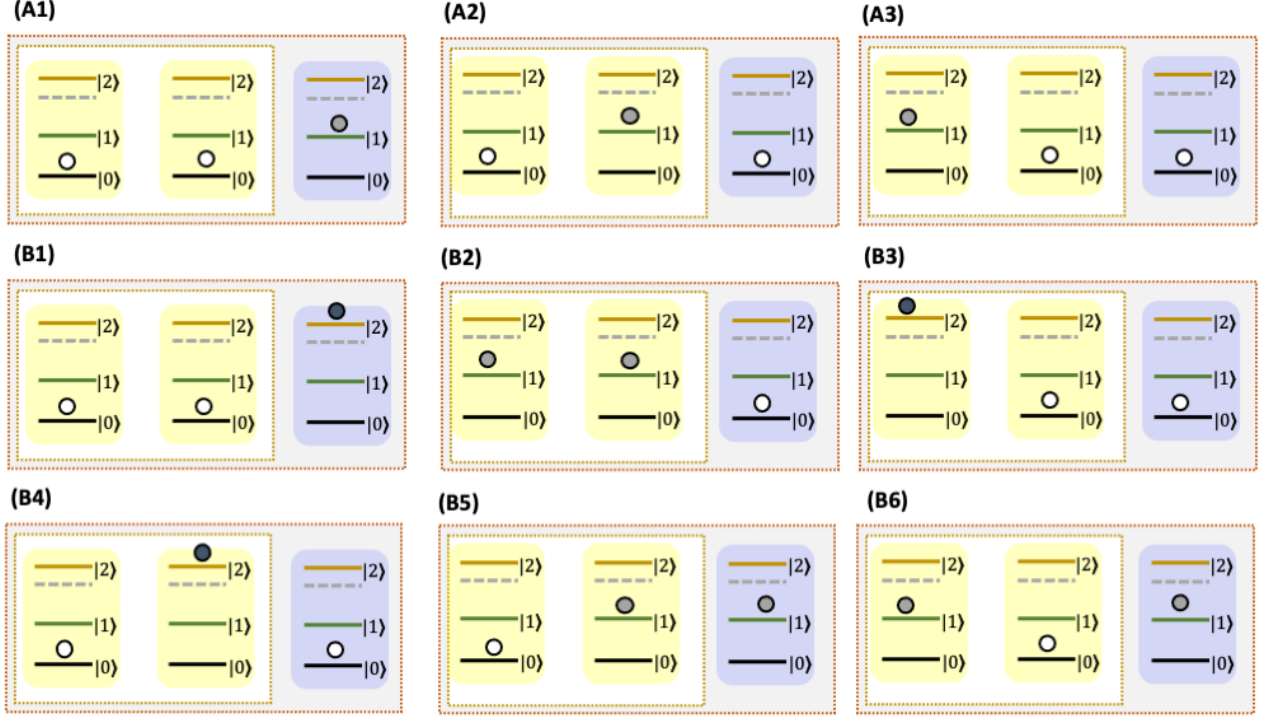


FIG. 3: Illustration of cavity-vibron configurations involved in mediating cavity-mediated vibrational excitation transfer pathways. The first row (A1-A3) represents single excitation exchange processes, while the second and third rows (B1-B6) represent two-excitation exchange processes. The gray (white) background underscores the configuration mixing facilitated by cavity-vibron (inter-vibron) coupling. The ground state corresponds to the absence of excitations. The one-polariton states comprise weighted contributions from three configurations: pure one-photon cavity (i.e., $|00\rangle|1\rangle_c$) or mixed cavity-vibron configurations (i.e., $|10\rangle|0\rangle_c, |01\rangle|0\rangle_c$). Due to the interplay of the coulomb-interaction mediated hopping and cavity interactions, these excitations are delocalized over vibron and cavity modes to varying degrees. The two-polariton states contains weighted contributions from six configurations: pure two-vibron states (i.e., $|20\rangle|0\rangle_c, |02\rangle|0\rangle_c, |11\rangle|0\rangle_c$), pure two-photon cavity states (i.e., $|00\rangle|2\rangle_c$), and mixed cavity-vibron configurations (i.e., $|10\rangle|1\rangle_c, |01\rangle|1\rangle_c$).

modes were maintained at a relative ratio of $g_{2,k}^{(b)}/g_{1,k}^{(b)} = 1.25$.

C. Vibron-polariton-phonon interactions

It is assumed that each vibron mode is independently coupled to a set of noninteracting phonon modes. It allows the construction of the generic spectral function of the phonon modes as

$$C_j(\omega) = \pi \sum_j d_j^2 \left(\delta(\omega - \omega_j) + (\omega + \omega_j) \right) \quad (4)$$

where ω_j , $d_j = S_j \omega_j$ represents the phonon mode frequencies and couplings respectively, with S_j being the Huang-Rhys factor. The spectral function of the extrinsic vibrational modes is described by one overdamped Brownian oscillator and structured Brownian oscillator. In the limit of continuous frequency distributions, the phonon spectral function takes the form.

$$J(\omega) = \frac{2\lambda_0 \gamma_0 \omega}{(\omega^2 + \gamma_0^2)} + \frac{2\lambda v^2 \gamma \omega}{((v^2 - \omega^2)^2 + \omega^2 \gamma^2)} \quad (5)$$

For the numerical simulation, the following parameters are used: $\lambda_0 = 15\text{cm}^{-1}$, $\gamma_0 = 20\text{cm}^{-1}$ for the overdamped oscillator, and $\lambda = 15\text{cm}^{-1}$, $v = 721\text{cm}^{-1}$ for the structured oscillator. The variables γ_0^{-1}, v^{-1} define the timescale

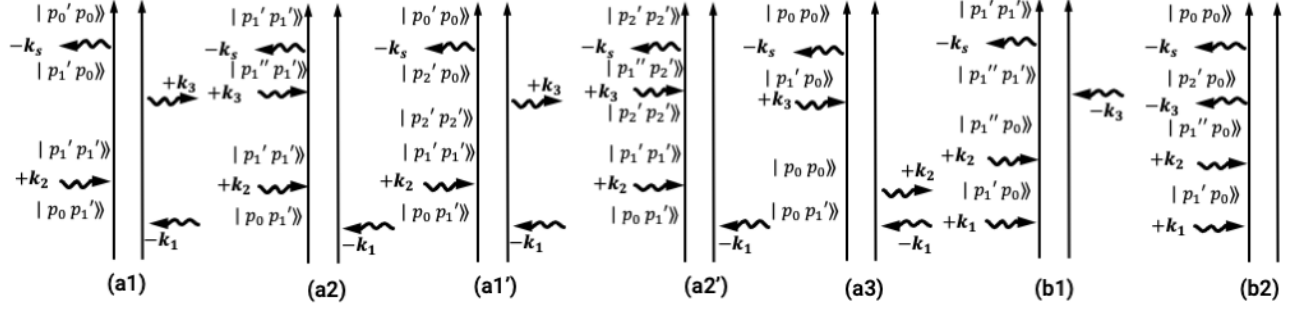


FIG. 4: The Liouville space Feynman diagrams can be used to rationalize the material origin of the signal. In the diagram, the time evolution is given by vertical pairs of arrows representing bra-ket, denoted $|ab\rangle \rightarrow |a\rangle\langle b|$. The wiggly lines pointing towards (away from) the vertical ones represent interaction with $-\omega(+k)(+\omega(-k))$ denoting absorption (emission) of a single excitation. The material states at each interval are denoted by $p_{ab}^{(n)}$ that indicates ab -the element of the density operator projected in the n -th polariton manifold. The five diagrams, labelled (a1) – (a3) and (a1'), (a2') denote pathways associated with the photon-echo signal while the rest, labelled ((b1) – (b2)) denote pathways associated with the double quantum coherence signal. The shaded area in (a1'), (a2') signifies phonon-induced polariton transport.

of the damping dynamics and can be estimated from the linear absorption and Fluorescence signals [20]. The time-dependent function that defines the dissipative kernel is given by,

$$\overline{C}_j^{(\pm)}(t) = \int_{-\infty}^{\infty} \frac{d\omega}{2\pi} C_j(\omega) \times [\coth(\beta\hbar\omega/2) \cos(\omega t) \mp i \sin(\omega t)] \quad (6)$$

Using the following definition

$$\overline{C}_j^{(\pm)}(\omega) = \int_0^{\infty} dt \exp(i\omega t) \overline{C}_j^{(\pm)}(t) \quad (7)$$

The phonon correlation function can be expressed as

$$\begin{aligned} C(\tau) &= (\lambda_0\gamma_0/2) \cot(\beta\gamma_0/2) \exp(-\gamma_0\tau) + \frac{\lambda}{2\zeta} \\ &\left(\coth(i\beta\phi^+/2) \exp(-\phi^+\tau) - \coth(i\beta\phi^-/2) \exp(-\phi^-\tau) \right) \\ &+ (-i\lambda_0\gamma_0/2) \exp(-\gamma_0\tau) + \frac{i\lambda v^2}{2\zeta} \left(\exp(-\phi^+\tau) - \right. \\ &\left. \exp(-\phi^-\tau) \right) - \sum_{n=1}^{\infty} \left((4\lambda\gamma v^2/\beta)(\nu_n/(v^2 + \nu_n^2)^2 - \nu_n^2\gamma^2) \right. \\ &\left. + (2\lambda_0\gamma_0/\beta)(\nu_n/(\nu_n^2 - \gamma_0^2)) \right) \exp(-i\nu_n\tau) \end{aligned} \quad (8)$$

Herein, $\phi^{\pm} = (\gamma/2) \pm i\zeta$ is defined, where $\zeta = \sqrt{(v^2 - \gamma^2/4)}$ and Matsubara frequencies, $\nu_n = n(2\pi/\beta)$, are introduced. Additionally, the parameter $\beta = 1/\kappa T$ is defined, where κ represents the Boltzmann constant κ and denotes the temperature T . The real and imaginary components of $\overline{C}_j^{(\pm)}(\omega)$ define the relaxation parameters and the spectral shift, respectively (Eq. B).

The overdamped Brownian oscillator spectral function is known to provide a good approximation of low energy modes in molecular liquids, solvents and can be adapted to accommodate a range of phonon modes. Such spectral functions effectively act as finite frequency bandwidth reservoirs. The phonons acting as reservoirs give rise to cavity-modulated intra-manifold vibron-polariton transport, relaxation, and inter- and intra-manifold dephasing. These effects can be captured by evaluating the relaxation kernel in the combined one and two-polariton basis. Due to the absence of reservoir-induced polariton number non-conserving transitions, the relaxation kernel factorizes in terms

of intra-manifold kernels. Given that the cavity energy scales are comparable to the inter-mode hopping and cavity dissipation is explicitly neglected, a Markovian description of dissipative dynamics is used. The relevant expressions are systematically derived in B. Typically, the Markovian formulation evaluates the relaxation parameters using formulas that can be interpreted as sampling the vibrational spectral function at specific energy gaps. This crucial aspect were highlighted for molecular aggregates before by the authors for more general spectral functions [20]. The one and two-polariton Green's functions are obtained using the following formulas for dephasing and relaxation and can be expressed as,

$$G_{p_1 p_2 p_3 p_4}^N(t) = \delta_{p_1 p_2} \delta_{p_3 p_4} \exp \left[-i\omega_{p_1 p_3} t - (\gamma_{p_1 p_3}^* + \frac{1}{2}(\Sigma_{p_1 p_1, p_1 p_1}^{(2)} + \Sigma_{p_3 p_3, p_3 p_3}^{(2)})t) \right] + (1 - \delta_{p_1 p_2}) \delta_{p_1 p_3} \delta_{p_2 p_4} \sum_r \chi_{p_1 r}^R D_{rr}^{-1} \exp(-\lambda_r t) \chi_{rp_3}^L \quad (9)$$

where the λ_r is the r -th eigenvalue of $\Sigma_{p_1 p_1, p_3 p_3}^{(2)}$ and χ^R/χ^L are the right and left eigenvectors which satisfies, $D_{rr} = \chi^L \chi^R$ and normalization condition is set by, $\chi^L \chi^R = 1$. As mentioned, the Green's function $G_{p_1 p_2, p_3 p_4}(t)$ characterizes the intra-manifold polariton transport (Fig. 7,8), dephasing and relaxation timescales, and will be useful in evaluating the signal expressions presented in the next section.

D. Vibron-polariton-laser interactions

The system is excited by an external laser in a cavity-pumping configuration. The laser is assumed to operate within a weak-field regime, promoting single-quantum transitions within its spectral bandwidth. The corresponding interaction Hamiltonian is expressed as

$$H_{\text{int}} = \sum_m E(t) \left(d_m a_k^\dagger + \sqrt{2} d_m a_k^\dagger a_k a_k + \text{c.c.} \right) \quad (10)$$

In the above, the total electric field $E(t) = \sum_j E_j(t)$, and the transition dipole parameter d_m are defined. The total field constituted of non-overlapping laser pulses, defined as

$$E(t) = \sum_j \mathcal{E}_j(t - \tau_j) \exp[i(\mathbf{k}_j \mathbf{r} - \omega_j(t - \tau_j))] + \text{c.c.} \quad (11)$$

The field profiles of the non-overlapping pulses are considered to be of the Gaussian form, specifically, $\mathcal{E}_{0,j}(t) = \exp(-\Gamma_{0,j}^2 t^2)$. Here, $\Gamma_{0,j}$ is related to the temporal width of the pulse $\tau_{0,j}$ via $\Gamma_{0,j} = 2\ln(2)/\tau_{0,j}$, where ω_j represents the frequency, \mathbf{k}_j the wavevector, and τ_j the centering time, respectively. These centering variables τ_j , are crucial for establishing the temporal ordering of the pulse sequences, as discussed in Appendices C and D. In the cavity-pumping configuration, the external laser induces resonant interaction between the polariton manifolds. In the tensor-product basis these interactions are mediated by the pure cavity modes. The tensor-product basis is transformed, using the transformation matrix given in Eq. (3) yielding the corresponding transition matrix elements between the polariton manifolds.

The weak-driving regime is suitable for the application of conventional MDCS techniques due to the favorable scaling of the signal with the intensity of the incoming fields. This regime ensures minimal perturbation to the vibron-polariton modes, allowing the probing of intrinsic energy scales of the system set by the cavity interactions. Furthermore, the low energy pumped into the vibron-polariton modes avoids external laser-induced non-linearity, and driving induced phonon dissipation [68–70]. Within the framework of the chosen model, the relative energy scales of the cavity-vibron and vibron-phonon coupling largely govern these aspects.

III. COHERENT MULTIDIMENSIONAL SIGNALS

A. Double-quantum coherence

To begin with, the focus is directed towards the signal that is capable of extracting information regarding the correlation between polariton states. The double-quantum coherence signal, generated in the phase-matching direction $\mathbf{k}_{\text{III}} = \mathbf{k}_1 + \mathbf{k}_2 - \mathbf{k}_3$, specifically probes the two-polariton resonances sensitive to cavity modulated $U^{(2)}$ couplings.

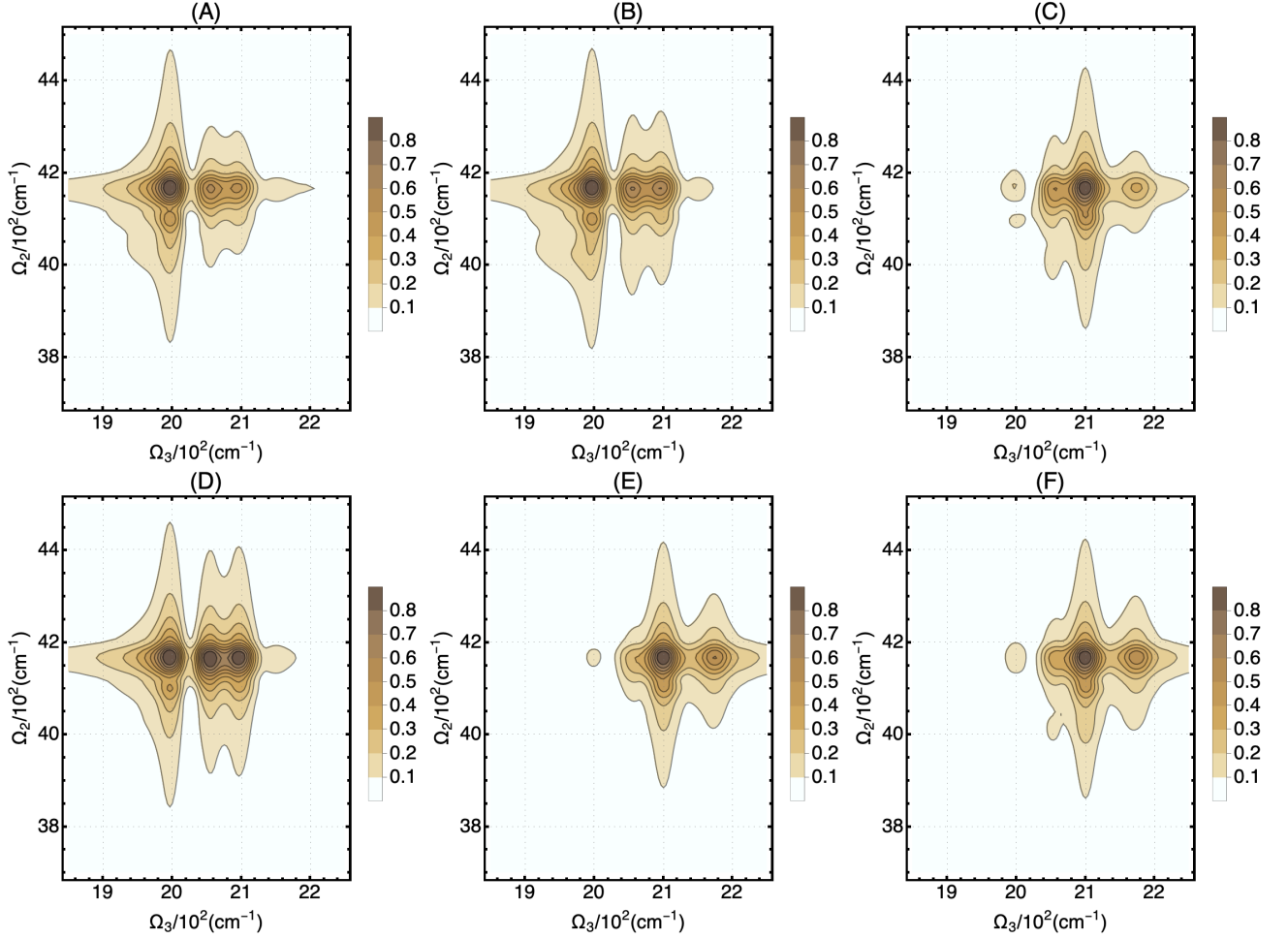


FIG. 5: Double-quantum coherence signal for $t_1 = 0$. The spectral features represent the correlation between the states, appearing in the form of one-polariton resonances. Corresponding pathways are given in Fig. 4. For parameters, see the discussion in section III A. In presenting (A)-(F), the temporal width of the excitation pulse, the excitation frequencies, and the final projection frequencies are varied. The signal, qualitatively, reflects the accumulation of spectral weights in few resonances. It was shown that careful selection of pulse parameters: temporal width and central frequencies, can indeed help amplify and suppress some of them. This holds true for across energy in the two-polariton manifold.

In the DQC technique, the two-polariton coherence is induced via the first two polariton-laser interactions. After evolving for a parametric time interval, the time-dependent polarization is projected onto two discriminating one-polariton coherence components. The differential nature of these two components determines the magnitude of the signal. The signal is derived in the Appendix D and expressed as

$$\begin{aligned}
 S_{\text{DQC}}(\Omega_2, \Omega_3) = & i^3 c_0 \times \sum_{p_2'' p_2' p_1' p_0} \frac{d_{p_1'' p_2'} \mathcal{E}_s^*(\omega_{p_1'' p_2'} - \omega_s) d_{p_2' p_0} \mathcal{E}_3^*(\omega_{p_2' p_0} - \omega_3) d_{p_1'' p_1'} \mathcal{E}_2(\omega_{p_1'' p_1'} - \omega_2) d_{p_1' p_0} \mathcal{E}_1(\omega_{p_1' p_0} - \omega_1)}{(\Omega_3 - z_{p_2'' p_2'})(\Omega_2 - z_{p_2' p_0})} \\
 & \times \exp(-i z_{p_1' p_0} t_1) - \frac{d_{p_1'' p_1'} \mathcal{E}_s^*(\omega_{p_1'' p_1'} - \omega_s) d_{p_2' p_0} \mathcal{E}_3^*(\omega_{p_2' p_0} - \omega_3) d_{p_1'' p_1'} \mathcal{E}_2(\omega_{p_1'' p_1'} - \omega_2) d_{p_1' p_0} \mathcal{E}_1(\omega_{p_1' p_0} - \omega_1)}{(\Omega_3 - z_{p_2' p_0})(\Omega_2 - z_{p_1' p_0})} \exp(-i z_{p_1' p_0} t_1) \}
 \end{aligned} \quad (12)$$

where frequency domain field profiles have been defined i.e., $\mathcal{E}_j(\omega) = \sqrt{\pi/\Gamma_{0,j}} \exp[-(\omega - \omega_{0,j})^2/4\Gamma_{0,i}]$. From the diagrams in Fig. 4, the signal can be interpreted as a result of interfering contributions arising from two pathways. The two-dimensional frequency correlation plots, presented in Fig. 5, are generated using two frequency variables, Ω_2

and Ω_3 . These Ω_j frequencies are Fourier conjugate variables of the respective time delay parameters, t_2 and t_3 . The emergent peaks, i.e., resonances appearing in the expression along Ω_2 and Ω_3 , can be monitored by scanning the axes. The signal reveals correlation effects via peak amplitudes and positions in the off-diagonal areas of the two-dimensional correlation plots. The DQC signal diminishes if the spectral weights associated with the two pathways linked to the variable Ω_3 are comparable in magnitude. The resonances along this axis may differ as a consequence of differential vibrational anharmonicity or cavity-mediated vibrational mode mixing.

For the double-quantum coherence signal, the simulation results, denoted (A)-(F), are presented in Fig. 5. Here, all simulations were performed by setting the first delay time to $t_1 = 0$, making the initial two interactions coincident. For the reference case presented in (A), the temporal width of the incoming and the heterodyning laser pulses are chosen as, $\tau_1 = \tau_2 = \tau_3 = 100$ fs, and $\tau_4 = 100$ fs, respectively. The central frequencies of the incoming and the heterodyning laser pulses are selected to coincide with specific transitions by setting $\omega_1 = \omega_{p'_2 p_0}$, $\omega_2 = \omega_{p'_2 p_0}$, $\omega_3 = E_{p'_5 p'_1}$, and $\omega_4 = \omega_{p'_5 p'_1}$, respectively. This choice indicates that the final two interactions preferentially project onto a specific energy sector (lower, in this instance). It is observed that four resonances within the region of $\{\Omega_2, \Omega_3\} \approx \{41.0 - 42.0, 19.7 - 21.0\} \times 10^2 \text{ cm}^{-1}$ are prominent, among which the off-diagonal resonances convey the correlation information. The remaining presented results incorporate parametric variations of this reference simulation. In (B), the role of broadband excitation is investigated by setting $\tau_4 = 40$ fs. The resulting signal reveals spectral narrowing of specific peaks ($\{\Omega_2, \Omega_3\} \approx \{41.8, 20.5 - 21.0\} \times 10^2 \text{ cm}^{-1}$) while the correlation pattern remains relatively unaltered. This observation is indicative of the fact that, given the specific choice of final state projections, the number of resonances involved did not undergo a fundamental change in character. To assess this observation, in (C), different projection frequencies are employed by setting $\omega_3 = \omega_4 = \omega_{p'_2 p'_1}$ while maintaining the other parameters consistent with (A). The resonances zones ($\{\Omega_2, \Omega_3\} \approx \{41.9, 21.0\} \times 10^2 \text{ cm}^{-1}$, and $\approx \{41.9, 21.7\} \times 10^2 \text{ cm}^{-1}$) in the spectra shift towards the higher end of the Ω_3 axis, indicating the prominent role of the final two interactions. In (D), the nature of different state initializations is investigated by setting the central frequencies of the excitation pulses as $\omega_1 = \omega_2 = \omega_{p'_3 p_0}$. In comparison to the equivalent scenario in (A), it is evident that the central peaks ($\{\Omega_2, \Omega_3\} \approx \{41.9, 20.5 - 21.5\} \times 10^2 \text{ cm}^{-1}$) have acquired considerable spectral weights. One of these peaks carries correlation information. It is pertinent to compare this observation with the simulation presented in (E), where both the initial excitation and final projection frequencies are altered. In (E), only one off-diagonal peak, reminiscent of (C), around $\{\Omega_2, \Omega_3\} \approx \{41.9, 21.0 - 22.0\} \times 10^2 \text{ cm}^{-1}$, persisted. The plot is comparatively featureless, indicating it to be a case where lesser number of distinct resonances were involved. Finally, in (F), the effect of a broadband pulse on the preceding simulation is explored. Although some broadening of spectral features ($\{\Omega_2, \Omega_3\} \approx \{41.9, 21.9 - 22.0\} \times 10^2 \text{ cm}^{-1}$) can be observed, the involvement of lesser number of resonances resulted in minimal spectral alterations. DQC signal involves two excited polariton state absorption pathways that can be distinguished during the third time interval, t_3 . Consequently, pulse shaping strategies can be implemented during the initial two polariton-laser interactions to generate the polarization that facilitates maximal discrimination between the pathway amplitudes.

B. Photon-echo

The photon-echo signal, generated in the phase-matching direction $\mathbf{k}_1 = -\mathbf{k}_1 + \mathbf{k}_2 + \mathbf{k}_3$, exhibits sensitivity to polariton ground state bleaching, excited polariton state absorption, and emission processes. This signal predominantly probes the one-polariton resonances that are sensitive to cavity-modulated J_{mn} couplings in Eq. 1. The derivation of the signal is detailed in Appendix D. It is noted that the polarization oscillations during the first and third time intervals possess opposite phases if the dephasing parameters exhibit comparable magnitudes. In instances where the energy gaps are of comparable magnitudes, the frequency factors may undergo cancellation, thereby generating a polariton echo. Within the scope of this analysis, this echo can only be generated when the transport matrix elements during the second time interval are negligible. The physical interpretation of these pathways is further clarified by looking at the accompanying diagram in Fig. 4. The diagrams (a1) and (a2) represent excited polariton state absorption and emission processes and are influenced by phonon-induced polariton transport, as illustrated in (a1'), and (a2'). The photon-echo signal is expressed as,

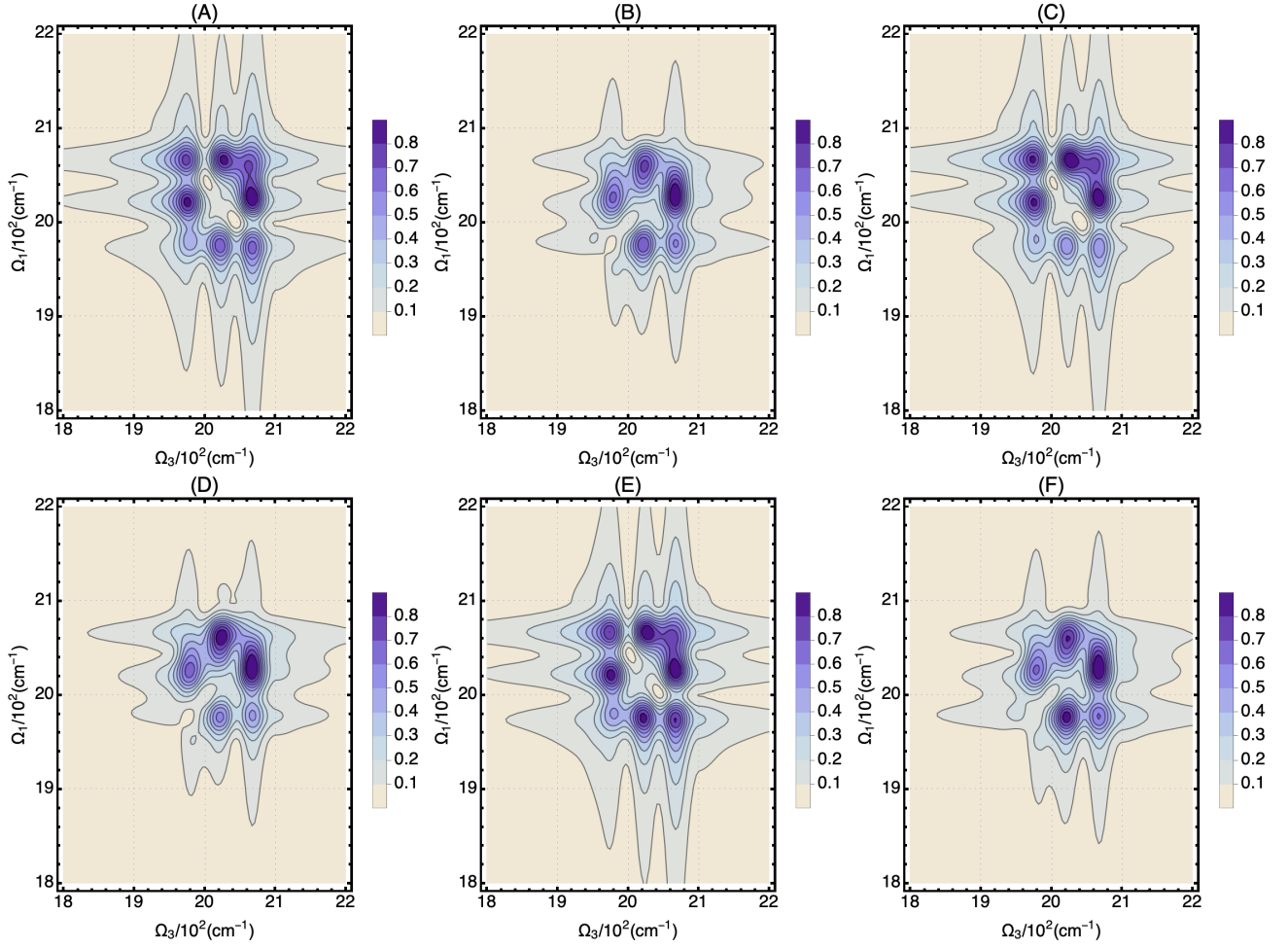


FIG. 6: Photon-echo signals for six parametric variations are illustrated for a specific cavity coupling strength and energy. The off-diagonal spectral features serve as correlation signatures, conventionally interpreted in terms of interacting one-polariton resonances. Detailed parameters and discussion can be found in section III B. The parametric variations investigated different one-polariton state initializations, distinct final polariton state projections, alterations in pulse duration, and dependencies on the waiting time. The expression presented in Eq. 13 and the diagram in 4 aid in the interpretation of these results.

$$\begin{aligned}
 S_{\text{PE}}(\Omega_1, \Omega_3) = i^3 c_0 \times & \left\{ \frac{d_{p_2'p_0}^* \mathcal{E}_s^*(\omega_{p_2'p_0} - \omega_s) d_{p_1'p_0} \mathcal{E}_3(\omega_{p_1'p_0} - \omega_3) d_{p_2'p_0} \mathcal{E}_2(\omega_{p_2'p_0} - \omega_2) d_{p_1'p_0}^* \mathcal{E}_1^*(\omega_{p_1'p_0} - \omega_1)}{(\Omega_3 - z_{p_2'p_0})(\Omega_1 - z_{p_0p_1'})} \right. \\
 & \times G_{p_4'p_3'p_2'p_1'}^{(N)}(t_2) + \frac{d_{p_2'p_0}^* \mathcal{E}_s^*(\omega_{p_2'p_0} - \omega_s) d_{p_2'p_0} \mathcal{E}_3(\omega_{p_2'p_0} - \omega_3) d_{p_1'p_0} \mathcal{E}_2(\omega_{p_1'p_0} - \omega_2) d_{p_1'p_0}^* \mathcal{E}_1^*(\omega_{p_1'p_0} - \omega_1)}{(\Omega_3 - z_{p_2'p_0})(\Omega_1 - z_{p_0p_1'})} G_{p_0p_0p_0p_0}^{(N)}(t_2) \\
 & \left. \frac{d_{p_1'p_1'}^* \mathcal{E}_s^*(\omega_{p_1'p_1'} - \omega_s) d_{p_1'p_2'} \mathcal{E}_3(\omega_{p_1'p_2'} - \omega_3) d_{p_2'p_1'} \mathcal{E}_2(\omega_{p_2'p_1'} - \omega_2) d_{p_1'p_0}^* \mathcal{E}_1^*(\omega_{p_1'p_0} - \omega_1)}{(\Omega_3 - z_{p_1'p_1'})(\Omega_1 - z_{p_0p_1'})} G_{p_4'p_3'p_2'p_1'}^{(N)}(t_2) \right\} \quad (13)
 \end{aligned}$$

where conventional notations were used for resonances, electric field profiles, and the Green's function. Herein, the signal is displayed using two scanning frequencies, Ω_1 and Ω_3 , for parametric values of delay time t_2 . The associated peaks correspond to the one-polariton resonances that can be generated through both ground-to-one-polariton and one-polariton-to-two-polariton transitions. The waiting time dependence is encoded within the matrix elements associated with $G_{p_1p_2p_3p_4}^{(N)}(t_2)$.

The results obtained from the numerical simulation are presented in Fig. 6, indexed (A)-(F). The simulation parameters for the reference run, (A), were as follows: the central frequencies of the incoming and the heterodyning laser pulses

were selected as $\omega_1 = E_{p'_2}$, $\omega_2 = E_{p'_2}$, $\omega_3 = E_{p'_2}$, and $\omega_4 = E_{p'_2}$, respectively; the temporal durations of the incoming and the heterodyning laser pulses were specified as $\tau_1 = \tau_2 = \tau_3 = 10$ fs and $\tau_4 = 10$ fs, respectively. The temporal delay parameter was set to $t_2 = 10$ fs. Three prominent resonance regions along Ω_3 can be observed, which can be further resolved along Ω_1 in three regions. The resonances situated around $\{\Omega_1, \Omega_3\} \approx \{20.2 - 20.5, 20.0 - 20.8\} \times 10^2 \text{cm}^{-1}$ carry the majority of the spectral weights. Keeping this parameter regime as a reference, several variations were explored to demonstrate the utility of this technique. In (B), the delay time is varied by setting $t_2 = 150$ fs to investigate the effects of phonon-induced polariton transport. The polariton transport timescales are indicative of the altered nature of the vibron mode energy transfer propensities. The corresponding plot reveals the coalescence of diagonal peaks and a diminished prominence or disappearance of off-diagonal peaks.

In (C), the central frequencies of the excitation pulse pairs are altered in an attempt to predominantly excite the one-polariton state p'_3 . Given that the waiting time remain the same as (A), a qualitative similarity with the former is noted. However, several distinctions can be observed: the lower energy resonances, specifically one diagonal and two off-diagonal resonances, exhibit decreased spectral weights ($\{\Omega_1, \Omega_3\} \approx \{19.8, 19.5 - 20.8\} \times 10^2 \text{cm}^{-1}$). Note that the two initially excited states are not significantly separated in energy, resulting in a uniform qualitative feature in the spectra. Subsequently, the delay time is varied to $t_2 = 150$ fs in (D) to monitor the effect of one-polariton transport given the newly excited initial state. It is noted that the resulting effects exhibit relative similarity yet are more pronounced in comparison to the (A)-(B) pair. This increased pronouncement can be observed by noting the coalescence and narrowing of the spectral peaks. The dependence on the transport timescales reveals that novel coherence features and frequency information are generated during the waiting times.

In (E), the temporal duration of the excitation pulses is altered to $\tau_0 = 40$ fs to facilitate broadband excitation of one-polariton states. The population redistribution at ultrashort times, as depicted in Fig. 7, presents an interesting scenario. All the features observed under narrowband excitation are present, albeit with differing spectral weights (e.g., an increase around the lower energy sector along Ω_1) in the plot, leading to the conclusion that the selectivity is diminished. To monitor the role of delay time dependence in this situation, in (F), $t_2 = 150$ fs is selected, and a distinct resonance region is observed along $\{\Omega_1, \Omega_3\} \approx \{19.7, 21.0\} \times 10^2 \text{cm}^{-1}$.

Upon comparing the behaviors observed at longer t_2 , indicative of transport timescales, a saturating trend may be noted. Even though the visible resonances carry distinct importance in each of these plots, uniform qualitative behavior can be observed. This uniformity can be attributed to the chosen parameters of the model. Specifically it can be attributed to an interplay between the corresponding value of the energy-gap sampled phonon spectral function and the transformation matrix elements of the two-polariton wavefunction.

IV. CONCLUSION

In this study, the dynamical role of mode nonlinearities in interacting vibrations under cavity interaction was investigated. To explore the role of cavity coupling, a parameter regime wherein the energy scales of inter-mode hopping and the effective cavity-vibration coupling strengths are comparable was the focus of this study. In previous investigations, this regime has received considerably less attention compared to the proverbial strong cavity coupling regime. The vibrational energy transport, which plays an important role in vibrational energy dispersal among the modes, originates due to the dipole-dipole interaction-induced hopping. The parameter domain examined in this article indicates a regime where governing the inter-vibrational mode energy redistribution process by localized resonator modes with specific electromagnetic field distributions may become feasible.

The role of the cavity-mediation in ultrafast vibrational energy transfer is quantified by the site-to-polariton basis transformation matrix elements, corresponding vibron-polariton state energies, and the relaxation parameters evaluated at the polariton energy gaps. Within the presented model, all these parameters are determined by the exact-diagonalization step, which mixes the inter-mode hopping and cavity-vibron coupling in a complex manner. The vibron-polariton resonances and their associated spectral weights carry the corresponding information into the expression for the signals. The complementary dynamical information can be revealed by jointly studying photon-echo and double quantum coherence signal. These signals were evaluated, and the spectra are displayed in terms of the two-dimensional frequency correlation plots, where diagonal and off-diagonal peaks convey distinct information about vibron-polariton resonances. By selecting the cavity frequency parameter to be within a small detuned regime, the role of the cavity in amplifying or suppressing certain dynamical polariton resonances associated with third-order response was revealed.

The cavity-induced modification of the bare-vibron properties gives rise to several dynamical features that can be thought of as the modified nonlinear response. These features originate from a modification of the finite-temperature cavity-matter equilibrium states, the nonlinearity of the dipolar transition operators, and cavity-induced changes in the long-range inter-mode coupling. All of them contribute towards the material mode anharmonicities which gives rise to the nonlinear response.

The phenomenological modeling, even though intuitive, faces several challenges. It is appreciated that the coupling between cavity modes and vibrations are not adequately captured by them. Consequently, there exist opportunities to integrate the presented theoretical framework with ab initio simulation methodologies. Several such proposals have already demonstrated early success in this direction [52, 53, 71–74]. They provide a computational framework for the evaluation of vibron-polariton nonlinear response.

The redistribution of vibrational energy in multimode vibrations often takes place in a non-statistical manner [75]. Spectroscopic investigation of multimode vibrons interacting with designer resonator modes would open up numerous opportunities to re-examine controlled intramolecular vibrational redistribution (IVR) and its significance in chemical reaction dynamics. Previously reported experimental studies on the cavity-mediated alteration of reaction rates have suggested a potential modification of the free-energy landscapes and rate constants [54, 76]. The MDCS techniques and parameter regime proposed herein may serve as a crucial operational probe in the time-frequency domain for investigating the signatures of such modification.

The characteristic mode dynamics investigated in this communication bear a close resemblance to the excitation regime of interacting carbonyl functional groups, which also play a crucial role in various catalytic processes. Monitoring the spectroscopic features of interacting carbonyl groups has aided in describing the underlying carbon-metal bonding dynamics and charge-transfer events. The dynamics of these functional groups within a cavity may be further complicated by the presence of disorder, which can be either static (arising from material inhomogeneity or spatial variations in cavity-matter coupling), or dynamic (originating from solvent or auxiliary vibrations) [77–82]. In such cases, spectroscopic investigation of the cavity-assisted dynamics will need a standardization for the groups to act as distinctive probed for the underlying matter dynamics.

The investigation of biomolecular dynamics and functionality is also facilitated by time-resolved X-ray diffraction (XRD) and nuclear magnetic resonance (NMR) spectroscopy. However, the ultrafast temporal resolution achievable through MDCS techniques exceeds the capabilities of these alternative methodologies, making MDCS a significant complementary tool [83–85].

Finally, I acknowledge a series of notable advancements in performing quantum nonlinear optical measurements on vibrational systems [86–88]. The presented theory can be readily adapted to explore these elaborate class of signals. Research in this direction is currently in progress and will be reported in subsequent publications.

Appendix A: Hamiltonian

Quasi-particle-based descriptor of the localized vibrations have been taken into account in previous works [16, 89–91]. The versatility of such a description stems from the fact that it provides a transparent understanding of the underlying physical processes, and the parameters were systematically estimated commencing from the ab-initio Hamiltonian. The first-quantized Hamiltonian of quantum nuclear dynamics within the Born–Oppenheimer approximation is well-established:

$$H = \frac{1}{2} \sum_m \frac{P_m^2}{M_m} + V(\mathbf{X}) \quad (\text{A1})$$

where $V(\mathbf{X}) = V(X_1, X_2, \dots)$ represents the multidimensional potential energy function. For anharmonic vibrational modes, the potential energy function can be expanded around the equilibrium geometry V_0 , yielding

$$\begin{aligned} H = & \frac{1}{2} \sum_m \left(\frac{P_m^2}{M_m} + M_m \omega_m^2 X_m^2 \right) + V_0 + \sum_m V_m X_m \\ & + \sum_{m \neq n} \frac{V_{mn}}{2!} X_m X_n + \sum_{mnk=1}^N \frac{V_{mnk}}{3!} X_m X_n X_k \\ & + \sum_{mmkl} \frac{V_{mmkl}}{4!} X_m X_n X_k X_l + \dots \end{aligned} \quad (\text{A2})$$

In the preceding expression, the X represent displacement coordinates. The terms denoted by V correspond to the derivatives of the potential energy surface (PES), representing effective force constants. One further define the operators,

$$\begin{aligned} X_m &= (1/\sqrt{2M_m\omega_m})(B_m^\dagger + B_m) \\ P_m &= -i\sqrt{M_m\omega_m/2}(B_m^\dagger - B_m) \end{aligned} \quad (\text{A3})$$

where $B_m^\dagger(B_m)$, the creation (annihilation) operators, follow the Bosonic commutation relations. Utilizing Bosonic quantization, the Hamiltonian can be recast as,

$$H_{\text{vibron},0} = \sum_{mn} U_{mn} B_m^\dagger B_n + \sum_{mnkl} U_{mnkl} B_m^\dagger B_n^\dagger B_k B_l + H_{\text{vibron},1} \quad (\text{A4})$$

where

$$\begin{aligned} H_{\text{vibron},1} = & \sum_{mn} U_{mn} B_m^\dagger B_n^\dagger + U_{mn} B_m B_n \\ & + \sum_{mnk} \left(U_{mnk} B_m^\dagger B_n^\dagger B_k^\dagger + U_{mn,k} B_m^\dagger B_n^\dagger B_k \right. \\ & \left. + U_{mnk} B_m^\dagger B_n B_k + U_{mnk} B_m B_n B_k \right) \\ & + \sum_{mnkl} \left(U_{mnk,l} B_m^\dagger B_n^\dagger B_k^\dagger B_l + U_{m,nkl} B_m^\dagger B_n B_k B_l \right. \\ & \left. + U_{mnkl} B_m^\dagger B_n^\dagger B_k^\dagger B_l^\dagger + U_{mnkl} B_m B_n B_k B_l \right) \end{aligned} \quad (\text{A5})$$

In the equation above, when representing the normal-ordered Hamiltonian, the expansion was truncated, and terms up to quartic order were retained, defining

$$\begin{aligned} U_{mn} = & \delta_{mn}(\omega_n + \frac{1}{2} \sum_l U_{nnll}) \\ & + \frac{1}{2}(1 - \delta_{mn}) \left(\frac{V_{mn}}{\sqrt{(M_m \omega_m)(M_n \omega_n)}} + \sum_{l=1}^N U_{mlnl} \right), \end{aligned} \quad (\text{A6})$$

and

$$\begin{aligned} U_{mnkl} = & \frac{1}{2!4!4} \sum_{\text{perm}(mnlk)} V_{mnlk} \\ & \frac{V_{mnlk}}{\sqrt{(M_m \omega_m)(M_n \omega_n)(M_l \omega_l)(M_k \omega_k)}} \end{aligned} \quad (\text{A7})$$

Furthermore, neglecting the number non-conserving terms results in the effective vibron Hamiltonian employed in the main text. Conventional treatments of cavity-free vibron dynamics often utilize the Hamiltonian obtained by exact diagonalization in the following form:

$$H_{\text{vibron}} = \sum_{\alpha^{(1)}} E_{\alpha^{(1)}} B_{\alpha^{(1)}}^\dagger B_{\alpha^{(1)}} + \sum_{\alpha^{(2)}} E_{\alpha^{(2)}} Y_{\alpha^{(2)}}^\dagger Y_{\alpha^{(2)}} \quad (\text{A8})$$

The one-vibron and two-vibron bases can be expressed as:

$$\begin{aligned} |\alpha^{(1)}\rangle & \equiv B_{\alpha^{(1)}}^\dagger |0\rangle = \sum_{m=1}^N \phi_{\alpha^{(1)},m}^{(1)} B_m^\dagger |0\rangle \\ |\alpha^{(2)}\rangle & \equiv Y_{\alpha^{(2)}}^\dagger |0\rangle = \sum_{mm=m}^N \phi_{\alpha^{(2)},mn}^{(2)} B_m^\dagger B_n^\dagger |0\rangle \end{aligned} \quad (\text{A9})$$

The neglected number non-conserving terms, when expressed in this basis, would generate transitions between the one- and two-vibron Hamiltonian blocks.

Appendix B: Dissipative polariton kinetics

In this section, the key equations that permit a simple yet adequate description of dissipative polariton kinetics for a general bath at thermodynamic equilibrium are presented. In the main text, the relaxation parameters necessary for

evaluating the signal were described. Herein, the expressions are systematically derived, starting from the Markovian relaxation kernel. The Markovian master equation for the reduced polariton density operator can be written as

$$\frac{d}{dt} \sigma_{ab} = -i[H_S, \sigma]_{ab} + \sum_{cd} K_{ab,cd} \sigma_{cd} \quad (\text{B1})$$

The relaxation kernel is given by

$$\begin{aligned} K_{a_4 a_3, a_2 a_1} &= \sum_j \lambda_j \{ \delta_{a_1 a_3} \sum_{e'} \bar{C}_j^{(+)}(\omega_{a_2 e'}) \\ &\times \Phi_{a_4 a' a_2 a'} + \delta_{a_4 a_2} \sum_{a'} \bar{C}_j^{(-)}(\omega_{a' a_1}) \Phi_{a' a_3 a' a_1} - \\ &\bar{C}_j^{(+)}(\omega_{a_2 a_4}) \Phi_{a_4 a_3 a_2 a_1} - \bar{C}_j^{(-)}(\omega_{a_3 a_1}) \Phi_{a_4 a_3 a_2 a_1} \} \end{aligned} \quad (\text{B2})$$

where

$$C_{a_4 a_3 a_1 a_1} = \sum_n T_{na_4} T_{na_3} T_{na_2} T_{na_1} \quad (\text{B3})$$

For the purposes of this analysis, the real part of the phonon correlation function

$$\text{Re} \bar{C}_j^{(\pm)}(\omega) = \frac{1}{2} C_j(\omega) [\coth(\beta \hbar \omega / 2) \pm 1], \quad (\text{B4})$$

allows one to determine the state-specific transport parameters

$$K_{a_2 a_2, a_1 a_1} = -2 \text{Re} \sum_j \lambda_j \bar{C}_j^{(+)}(\omega_{a_1 a_2}) \Phi_{a_2 a_2 a_1 a_1}, \quad (\text{B5})$$

and state specific dephasing parameters

$$\gamma_{a_1} = \sum_j \lambda_j \sum_{a_2} \bar{C}_j^{(+)}(\omega_{a_1 a_2}) \Phi_{a_1 a_1 a_2 a_2} \quad (\text{B6})$$

In this work, the time-dependent dynamics of the polariton density operator is characterized by the Markovian description in the secular limit, meaning that the coherence (off-diagonal matrix elements in the polariton basis) and population (diagonal matrix elements in the polariton basis) terms are dynamically decoupled. The population terms follow the kinetic equation:

$$\frac{d}{dt} \rho_{a_2 a_2}(t) = - \sum_{a_1} K_{a_2 a_2, a_1 a_1} \rho_{a_1 a_1}(t), \quad (\text{B7})$$

In the equation above, the rate matrix form can be identified, provided the matrix elements obey the following constraints of probability conservation and detailed balance, expressed as:

$$K_{a_2 a_2, a_1 a_1} / K_{a_1 a_1, a_2 a_2} = \exp(-\omega_{a_2 a_1} / (k_B T)) \quad (\text{B8})$$

and $\sum_{a_1} K_{a_1 a_1, a_2 a_2} = 0$. The population terms describe the polariton transport resulting from the interaction with phonons. This is captured by the Green's function

$$\begin{aligned} G_{a_2 a_2, a_1 a_1}^{(N)}(t) &= [\exp(-Kt)]_{a_2 a_2, a_1 a_1} \\ &\equiv \sum_r \chi_{a_2 r}^{(R)} D_{rr}^{-1} \exp(-\lambda_r t) \chi_{r a_1}^{(L)}, \end{aligned} \quad (\text{B9})$$

The coherence terms, on the other hand, follow the kinetic equation:

$$\frac{d}{dt} \rho_{a_1 a_2}(t) = [-i\omega_{a_1 a_2} - \gamma_{a_1 a_2}^{(N)}] \rho_{a_1 a_2}(t), a_1 \neq a_2, \quad (\text{B10})$$

The corresponding Green's function is given by,

$$G_{a_1 a_2}(t) = \exp[-i\omega_{a_1 a_2} t - \gamma_{a_1 a_2}^{(N)} t] \quad (\text{B11})$$

where the dephasing parameter is defined as:

$$\gamma_{a_1 a_2}^{(N)} = \frac{1}{2}(K_{a_1 a_1, a_1 a_1} + K_{a_2 a_2, a_2 a_2}) + \tilde{\gamma}_{a_1 a_2}. \quad (\text{B12})$$

The pure dephasing parameter, $\tilde{\gamma}_{a_1 a_2}$, can be estimated, and corroborated from experiments. Both of these Green's function components can be combined and expressed in a compact form, as presented in the main text in Eq. 9. Along with these intra-manifold relaxation parameters, the inter-manifold line-broadening functions are defined as $\gamma_{a'_1 a_2} = (\gamma_{a'_1} + \gamma_{a_2})/2$. Finally, the inter-manifold Green's functions relevant for dephasing are obtained as:

$$G_{a'_1 a_2, a'_1 a_2}(t) = \exp[-i\omega_{a'_1 a_2} t - \gamma_{a'_1 a_2} t] \quad (\text{B13})$$

The presented results can be readily extended to out-of-equilibrium phonon modes and to scenarios where cavity dissipation is explicitly considered.

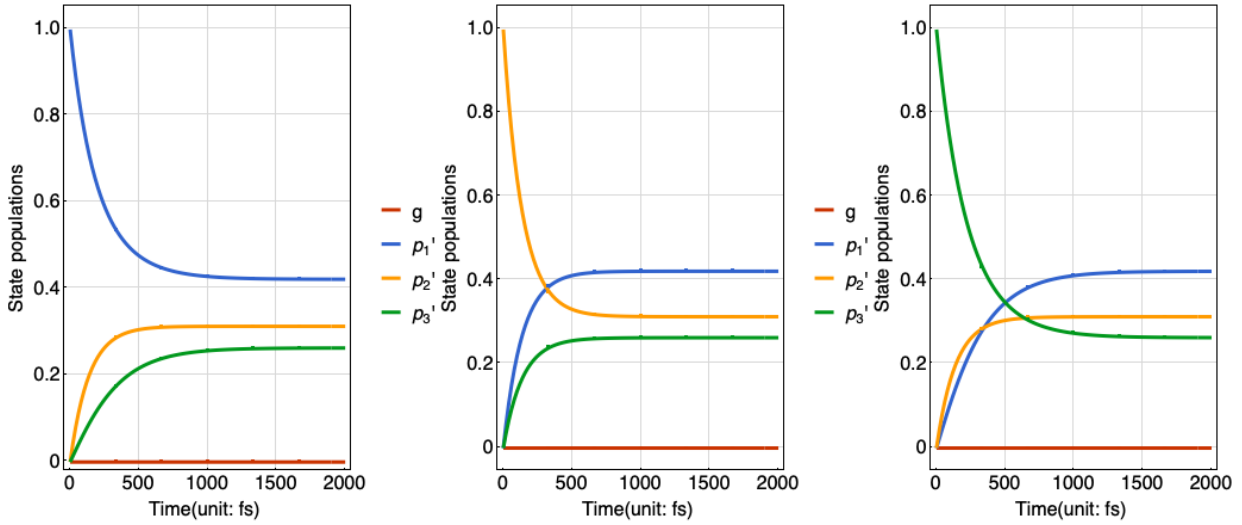


FIG. 7: Markovian population dynamics of one-polariton states are presented, illustrating the initial excitation in each of the three states within that manifold. In the absence of external driving and higher-order vibron anharmonicities, the polariton number-conserving manifolds remain decoupled. The onset of saturation of the population redistribution is observed around $t = 1.5\text{ps}$.

Appendix C: Nonlinear response formalism with finite pulses

In this section, a concise description containing essential steps of the derivation leading up to the expressions of the signals presented in the main text is provided.

The n -th order nonlinear polarization is defined as,

$$P^{(n)} = \text{Tr}[d\rho^{(n)}]$$

where $\rho^{(n)}$ represents the n -th order laser-perturbed density operator of the cavity-vibron system, given by

$$\begin{aligned} \rho(t) = & G(t)\rho(0) + \sum_{n=1}^{\infty} (-i)^n \int_0^t d\tau_n \cdots \int_0^{\tau_2} d\tau_1 \times \\ & G(t - \tau_n)L_{\text{int},-}(\tau_n) \cdots G(\tau_2 - \tau_1)L_{\text{int}}(\tau_1)G(\tau_1)\rho(0) \end{aligned} \quad (\text{C1})$$

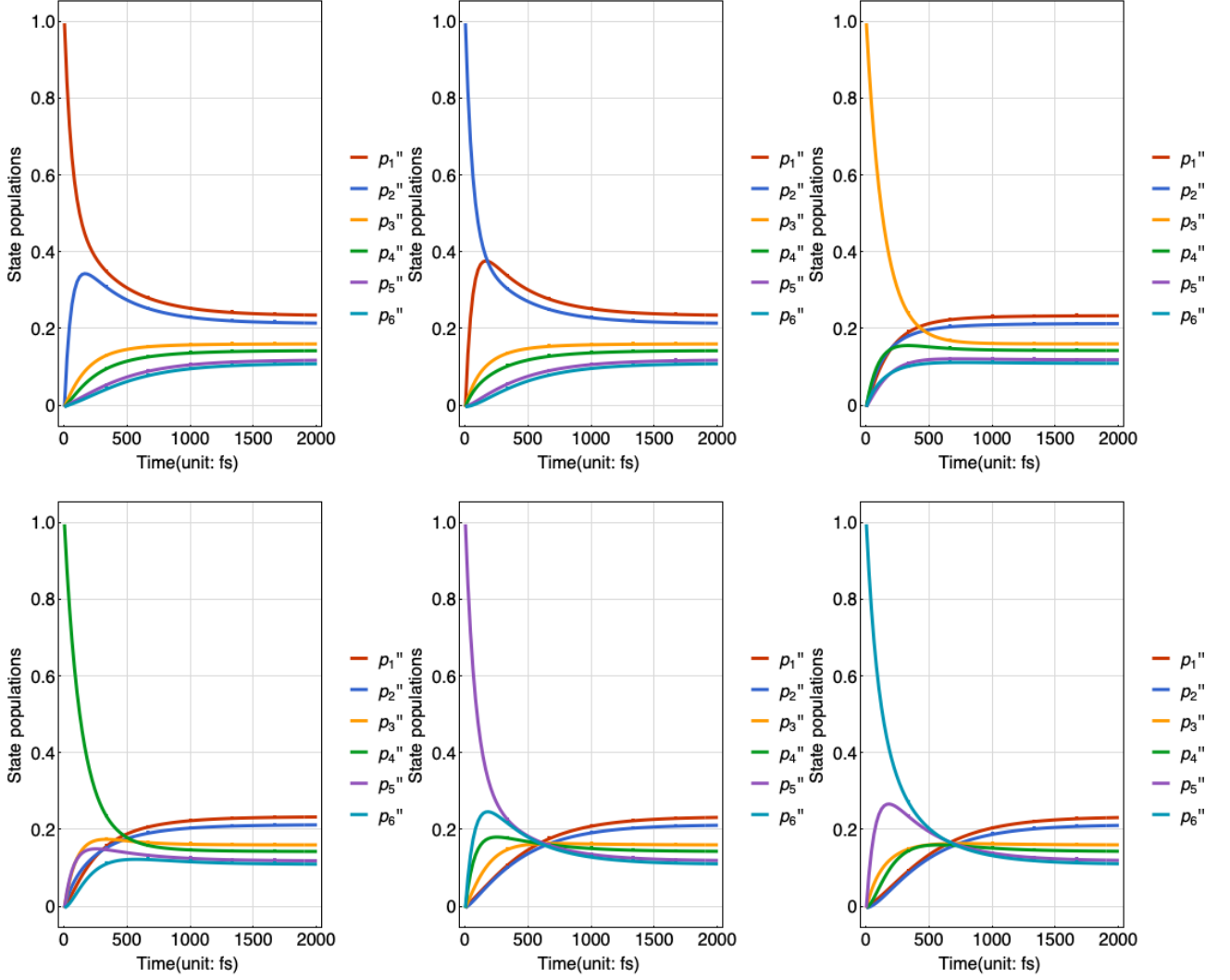


FIG. 8: Markovian population dynamics of two-polariton states are depicted, illustrating the initial excitation of six states within that manifold. Population transfer to the one-polariton manifold is prohibited due to the absence of coupling between these manifolds in an undriven system. Notably, the population redistribution beyond $t = 1.5$ ps shows no appreciable change. A variation in the characteristic time-scale of the population decay for each initial state is clearly observed.

This evolution is driven by the external laser, which interacts with the system via the dipole superoperator expressed as $L_{\text{int},-}O = [H_{\text{int}}, O]$. The incoming laser fields are represented as follows

$$E(t) = \sum_{j,u_j=\pm 1} \mathcal{E}_j^{u_j}(t - \tau_j) \exp[iu_j(\mathbf{k}_j \mathbf{r} - \omega_j(t - \tau_j))] + \text{c.c.} \quad (\text{C2})$$

Here, the complex field profile function of the j -th pulse, possessing frequency ω_j , wavevector \mathbf{k}_j , and centering time τ_j , is given by $\mathcal{E}_j^{u_j}(t - \tau_j)$. The indices u_j represent the distinct frequency components of the field and will be instrumental in deriving the final expressions of the signal. Utilizing the perturbative expansion outlined above, one can derive the expression for the third-order ($n = 3$) polarization. The latter can be induced by three incoming laser pulses satisfying the phase-matching condition $\mathbf{k}_s = \pm \mathbf{k}_3 \pm \mathbf{k}_2 \pm \mathbf{k}_1$. Employing these expressions for the field profiles, it is feasible to derive a compact expression for the third-order polarization

$$P^{(3)}(\mathbf{r}, t) = \sum_{\mathbf{k}_s} P_{\mathbf{k}_s}^{(3)}(t) \exp[i(\mathbf{k}_s \mathbf{r})]$$

where

$$\begin{aligned}
P_{\mathbf{k}_s}^{(3)}(t) = & \exp[-i\omega_s T_3 - i(u_2\omega_2 + u_1\omega_1)T_2 - iu_1\omega_1 T_1] \int_0^\infty \int_0^\infty \int_0^\infty dt_3 dt_2 dt_1 R_{\mathbf{k}_s}^{(3)}(t_3, t_2, t_1) \times \\
& \exp[i\omega_s t_3 + i(u_2\omega_2 + u_1\omega_1)t_2 + iu_1\omega_1 t_1] \\
& \mathcal{E}_3^{u_3}(t - t_3 - \tau_3) \mathcal{E}_2^{u_2}(t - t_3 - t_2 - \tau_2) \\
& \mathcal{E}_1^{u_1}(t - t_3 - t_2 - t_1 - \tau_1)
\end{aligned} \tag{C3}$$

Here, $t_j = \tau_{j+1} - \tau_j$ represent the controllable delays between the incoming laser pulses, and $R^{(3)}(t_3, t_2, t_1)$ denotes the time-domain response function for the cavity-vibron system. Within this formalism, the response functions encompass all the effects originating from the cavity-vibron-phonon interactions.

Appendix D: Time-domain nonlinear response functions: photon-echo and double quantum coherence

In the main text, the photon-echo (\mathbf{k}_I) and double quantum coherence (\mathbf{k}_{III}) signal, which are typically generated in the phase-matching direction $\mathbf{k}_I = -\mathbf{k}_1 + \mathbf{k}_2 + \mathbf{k}_3$ and $\mathbf{k}_{III} = +\mathbf{k}_1 + \mathbf{k}_2 - \mathbf{k}_1$, respectively, were presented. Here, the time-domain response functions corresponding to these signals are presented. The response functions are expanded in the field-free eigenbasis of the system, which is determined using the exact-diagonalization approach. This approach, while often numerically burdensome for large systems, possesses the advantage of allowing a straightforward and proper characterization of the initial state. The initial state in the polariton basis contains significant information regarding vibron-cavity correlation encoded in the respective energy values and transformation matrix elements Eq. 3. In the absence of a numerically tractable Hamiltonian, one may have to resort to a variational search for the initial equilibrium density operator.

The photon echo signal, in the time-domain representation can be expressed as

$$\begin{aligned}
R_{\mathbf{k}_I}(t_3, t_2, t_1) = & i^3 \theta(t_1) \theta(t_2) \theta(t_3) \sum_{p'_4 p'_3 p'_2 p'_1} \mu_{p_0 p'_4} \mu_{p'_3 p_0} \mu_{p'_2 p_0} \mu_{p_0 p'_1} \exp(-iz_{p'_4 p_0} t_3 - iz_{p_0 p'_1} t_1) G_{p'_4 p'_3 p'_2 p'_1}^N(t_2) \\
& + i^3 \theta(t_1) \theta(t_2) \theta(t_3) \sum_{p'_4, p'_1} \mu_{p_0 p'_4} \mu_{p'_4 p_0} \mu_{p'_1 p_0} \mu_{p_0 p'_1} \exp(-iz_{p'_4 p_0} t_3 - iz_{p_0 p'_1} t_1) \\
& - i^3 \theta(t_1) \theta(t_2) \theta(t_3) \sum_{p'_1 p'_4 p'_3 p'_2 p'_1} \mu_{p'_3 p_0} \mu_{p'_1 p'_4} \mu_{p'_2 p_0} \mu_{p_0 p'_1} \exp(-iz_{p'_1 p'_4} t_3 - iz_{p_0 p'_1} t_1) G_{p'_4 p'_3 p'_2 p'_1}^N(t_2)
\end{aligned} \tag{D1}$$

The contribution of three pathways (or five when considering the generalized form of the Green's function) to the signal is evident in the derived expressions. The diagrams displayed in Fig. 4 serve to rationalize these expressions. On the other hand, the double quantum coherence signal, in the time-domain representation, is expressed as,

$$\begin{aligned}
R_{\mathbf{k}_{III}}(t_3, t_2, t_1) = & -i^3 \theta(t_1) \theta(t_2) \theta(t_3) \sum d_{p'_2 p'_1} d_{p_0 p'_2} d_{p'_1 p'_1} d_{p'_1 p_0} \exp(-iz_{p'_1 p'_2} t_3 - iz_{p'_1 p_0} t_2 - iz_{p'_1 p_0} t_1) \\
& + i^3 \theta(t_1) \theta(t_2) \theta(t_3) \sum d_{p_0 p'_2} d_{p'_2 p'_1} d_{p'_1 p'_1} d_{p'_1 p_0} \exp(-iz_{p'_2 p_0} t_3 - iz_{p'_1 p_0} t_2 - iz_{p'_1 p_0} t_1)
\end{aligned} \tag{D2}$$

The signal contains two pathways that can be read off from the diagrams in Fig. 4.

Appendix E: Two-dimensional signal

The third-order heterodyne-detected signal is given by,

$$S(T_3, T_2, T_1) = \int_{-\infty}^{\infty} dt P_{\mathbf{k}_s}^{(3)}(t) E_s^*(t - \tau_s), \tag{E1}$$

Herein, $T_3 = \tau_s - \tau_3$, $T_2 = \tau_3 - \tau_2$, and $T_1 = \tau_2 - \tau_1$ are defined as the controllable time delay variables. The local-oscillator field used for heterodyning is given by the term, $E_s^*(t - \tau_s)$. The multidimensional spectrum is obtained by

taking a joint Fourier transform with respect to the time delays. This can be formally expressed as

$$S_{\mathbf{k}_s}^{(3)}(\Omega_3, \Omega_2, \Omega_1) = \int_0^\infty dT_3 \int_0^\infty dT_2 \int_0^\infty dT_1 \exp[i\Omega_3 T_3 + i\Omega_2 T_2 + i\Omega_1 T_1] S_{\mathbf{k}_s}^{(3)}(T_3, T_2, T_1) \quad (\text{E2})$$

The two-dimensional representation used in this article would involve choosing two time delays, which for the case of PE involves T_1, T_3 and for the case of DQC involves T_2, T_3 . The resulting representations are given in Eq. (12) and Eq. (13), respectively, which are obtained with the assumption that incoming pulses are well separated.

ACKNOWLEDGMENTS

A.D. acknowledges support from DESY (Hamburg, Germany), a member of the Helmholtz Association HGF. A.D. also acknowledges engaging in technical discussions with A. Rubio (MPSD, Hamburg) regarding ab-initio simulation algorithms of vibron-polariton dynamics and response theories.

-
- [1] M. Khalil, N. Demirdöven, and A. Tokmakoff, Coherent 2d ir spectroscopy: Molecular structure and dynamics in solution, *The Journal of Physical Chemistry A* **107**, 5258 (2003).
 - [2] M. Khalil, N. Demirdöven, and A. Tokmakoff, Obtaining absorptive line shapes in two-dimensional infrared vibrational correlation spectra, *Physical review letters* **90**, 047401 (2003).
 - [3] O. Golonzka, M. Khalil, N. Demirdöven, and A. Tokmakoff, Vibrational anharmonicities revealed by coherent two-dimensional infrared spectroscopy, *Physical review letters* **86**, 2154 (2001).
 - [4] N. Demirdöven, M. Khalil, and A. Tokmakoff, Correlated vibrational dynamics revealed by two-dimensional infrared spectroscopy, *Physical review letters* **89**, 237401 (2002).
 - [5] C. R. Baiz, B. Błasiak, J. Bredenbeck, M. Cho, J.-H. Choi, S. A. Corcelli, A. G. Dijkstra, C.-J. Feng, S. Garrett-Roe, N.-H. Ge, *et al.*, Vibrational spectroscopic map, vibrational spectroscopy, and intermolecular interaction, *Chemical reviews* **120**, 7152 (2020).
 - [6] B. Xiang and W. Xiong, Molecular vibrational polariton: Its dynamics and potentials in novel chemistry and quantum technology, *The Journal of Chemical Physics* **155** (2021).
 - [7] A. Debnath, *Dynamics and control of open quantum systems: applications to exciton dynamics in quantum dots and vibrational dynamics in carboxyhemoglobin*, Ph.D. thesis, Université de Toulouse, Université Toulouse III-Paul Sabatier (2013).
 - [8] C. Falvo, A. Debnath, and C. Meier, Vibrational ladder climbing in carboxy-hemoglobin: Effects of the protein environment, *The Journal of Chemical Physics* **138** (2013).
 - [9] P. Nuernberger, T. Vieille, C. Ventalon, and M. Joffre, *The Journal of Physical Chemistry B* **115**, 5554 (2011).
 - [10] C. Ventalon, J. M. Fraser, M. H. Vos, A. Alexandrou, J.-L. Martin, and M. Joffre, *Proceedings of the National Academy of Sciences* **101**, 13216 (2004).
 - [11] C. Falvo, L. Daniault, T. Vieille, V. Kemlin, J.-C. Lambry, C. Meier, M. H. Vos, A. Bonvalet, and M. Joffre, Ultrafast dynamics of carboxy-hemoglobin: Two-dimensional infrared spectroscopy experiments and simulations, *The Journal of Physical Chemistry Letters* **6**, 2216 (2015).
 - [12] K. Everitt, E. Geva, and J. Skinner, Determining the solvation correlation function from three-pulse photon echoes in liquids, *The Journal of chemical physics* **114**, 1326 (2001).
 - [13] Y. Tanimura and S. Mukamel, Two-dimensional femtosecond vibrational spectroscopy of liquids, *The Journal of chemical physics* **99**, 9496 (1993).
 - [14] A. Ishizaki and Y. Tanimura, Dynamics of a multimode system coupled to multiple heat baths probed by two-dimensional infrared spectroscopy, *The Journal of Physical Chemistry A* **111**, 9269 (2007).
 - [15] M. Dantus, Coherent nonlinear spectroscopy: from femtosecond dynamics to control, *Annual review of physical chemistry* **52**, 639 (2001).
 - [16] S. Mukamel, Femtosecond optical spectroscopy: a direct look at elementary chemical events, *Annual Review of Physical Chemistry* **41**, 647 (1990).
 - [17] S. Kushida, K. Wang, C. Genet, and T. W. Ebbesen, Ultrafast dynamics of solute molecules probed by resonant optical kerr effect spectroscopy, *The Journal of Physical Chemistry Letters* **13**, 9309 (2022).
 - [18] C. T. Middleton, A. M. Woys, S. S. Mukherjee, and M. T. Zanni, Residue-specific structural kinetics of proteins through the union of isotope labeling, mid-ir pulse shaping, and coherent 2d ir spectroscopy, *Methods* **52**, 12 (2010).
 - [19] A. Ghosh, J. S. Ostrander, and M. T. Zanni, Watching proteins wiggle: mapping structures with two-dimensional infrared spectroscopy, *Chemical reviews* **117**, 10726 (2017).
 - [20] S. Mukamel, *Principles of Nonlinear Optical Spectroscopy* (Oxford University Press, 1995).
 - [21] P. Hamm and M. Zanni, *Concepts and methods of 2D infrared spectroscopy* (Cambridge University Press, 2011).

- [22] M. Cho, *Two-dimensional optical spectroscopy* (CRC press, 2009).
- [23] J. C. Wright, N. J. Condon, K. M. Murdoch, D. M. Besemann, and K. A. Meyer, Quantitative modeling of nonlinear processes in coherent two-dimensional vibrational spectroscopy, *The Journal of Physical Chemistry A* **107**, 8166 (2003).
- [24] J. C. Wright, Multiresonant coherent multidimensional spectroscopy, *Annual review of physical chemistry* **62**, 209 (2011).
- [25] C. R. Baiz, P. L. McRobbie, J. M. Anna, E. Geva, and K. J. Kubarych, Two-dimensional infrared spectroscopy of metal carbonyls, *Accounts of chemical research* **42**, 1395 (2009).
- [26] C. R. Baiz, K. J. Kubarych, E. Geva, and E. L. Sibert III, Local-mode approach to modeling multidimensional infrared spectra of metal carbonyls, *The Journal of Physical Chemistry A* **115**, 5354 (2011).
- [27] C. R. Baiz, K. J. Kubarych, and E. Geva, Molecular theory and simulation of coherence transfer in metal carbonyls and its signature on multidimensional infrared spectra, *The Journal of Physical Chemistry B* **115**, 5322 (2011).
- [28] M. J. Nee, C. R. Baiz, J. M. Anna, R. McCanne, and K. J. Kubarych, Multilevel vibrational coherence transfer and wavepacket dynamics probed with multidimensional ir spectroscopy, *The Journal of chemical physics* **129** (2008).
- [29] K. Okumura and Y. Tanimura, Femtosecond two-dimensional spectroscopy from anharmonic vibrational modes of molecules in the condensed phase, *The Journal of chemical physics* **107**, 2267 (1997).
- [30] J. Nobakht, A. Pscherer, J. Renger, S. Götzinger, and V. Sandoghdar, Cavity-mediated hybridization of several molecules in the strong coupling regime, arXiv preprint arXiv:2501.00414 (2024).
- [31] Z. T. Brawley, S. Pannir-Sivajothi, J. E. Yim, Y. R. Poh, J. Yuen-Zhou, and M. Sheldon, Vibrational weak and strong coupling modify a chemical reaction via cavity-mediated radiative energy transfer, *Nature Chemistry* , 1 (2025).
- [32] A. Koner, M. Du, S. Pannir-Sivajothi, R. H. Goldsmith, and J. Yuen-Zhou, A path towards single molecule vibrational strong coupling in a fabry-pérot microcavity, *Chemical Science* **14**, 7753 (2023).
- [33] J. B. Pérez-Sánchez, A. Koner, N. P. Stern, and J. Yuen-Zhou, Simulating molecular polaritons in the collective regime using few-molecule models, *Proceedings of the National Academy of Sciences* **120**, e2219223120 (2023).
- [34] D. Wang, H. Kelkar, D. Martín-Cano, T. Utikal, S. Götzinger, and V. Sandoghdar, Coherent coupling of a single molecule to a scanning fabry-perot microcavity, *Physical Review X* **7**, 021014 (2017).
- [35] B. Gurlek, V. Sandoghdar, and D. Martín-Cano, Manipulation of quenching in nanoantenna-emitter systems enabled by external detuned cavities: a path to enhance strong-coupling, *ACS Photonics* **5**, 456 (2018).
- [36] A. Debnath and A. Rubio, Entangled photon assisted multidimensional nonlinear optics of exciton-polaritons, *Journal of Applied Physics* **128** (2020).
- [37] A. Debnath and A. Rubio, Entangled biphoton enhanced double quantum coherence signal as a probe for cavity polariton correlations in presence of phonon induced dephasing, *Frontiers in Physics* **10**, 879113 (2022).
- [38] X. Li, A. Mandal, and P. Huo, Cavity frequency-dependent theory for vibrational polariton chemistry, *Nature communications* **12**, 1315 (2021).
- [39] J. Levinsen, G. Li, and M. M. Parish, Microscopic description of exciton-polaritons in microcavities, *Physical Review Research* **1**, 033120 (2019).
- [40] A. D. Dunkelberger, B. S. Simpkins, I. Vurgaftman, and J. C. Owrutsky, Vibration-cavity polariton chemistry and dynamics, *Annual review of physical chemistry* **73**, 429 (2022).
- [41] T. E. Li, A. Nitzan, and J. E. Subotnik, Energy-efficient pathway for selectively exciting solute molecules to high vibrational states via solvent vibration-polariton pumping, *Nature communications* **13**, 4203 (2022).
- [42] T. E. Li, B. Cui, J. E. Subotnik, and A. Nitzan, Molecular polaritonics: Chemical dynamics under strong light-matter coupling, *Annual review of physical chemistry* **73**, 43 (2022).
- [43] T. E. Li, A. Nitzan, and J. E. Subotnik, Polariton relaxation under vibrational strong coupling: Comparing cavity molecular dynamics simulations against fermi’s golden rule rate, *The Journal of Chemical Physics* **156** (2022).
- [44] D. M. Juraschek, T. Neuman, J. Flick, and P. Narang, Cavity control of nonlinear phononics, *Physical Review Research* **3**, L032046 (2021).
- [45] D. N. Basov, A. Asenjo-Garcia, P. J. Schuck, X. Zhu, and A. Rubio, Polariton panorama, *Nanophotonics* **10**, 549 (2021).
- [46] C. Schäfer, J. Flick, E. Ronca, P. Narang, and A. Rubio, Shining light on the microscopic resonant mechanism responsible for cavity-mediated chemical reactivity, *Nature Communications* **13**, 7817 (2022).
- [47] J. Flick, M. Ruggenthaler, H. Appel, and A. Rubio, Atoms and molecules in cavities, from weak to strong coupling in quantum-electrodynamics (qed) chemistry, *Proceedings of the National Academy of Sciences* **114**, 3026 (2017).
- [48] M. Kowalewski, K. Bennett, and S. Mukamel, Cavity femtochemistry: Manipulating nonadiabatic dynamics at avoided crossings, *The journal of physical chemistry letters* **7**, 2050 (2016).
- [49] L. Chen, A. P. Fidler, A. M. McKillop, and M. L. Weichman, Exploring the impact of vibrational cavity coupling strength on ultrafast $\text{cn}^+ + \text{c-c6h}_{12}$ reaction dynamics, *Nanophotonics* **13**, 2591 (2024).
- [50] A. D. Wright, J. C. Nelson, and M. L. Weichman, A versatile platform for gas-phase molecular polaritonics, *The Journal of Chemical Physics* **159** (2023).
- [51] K. Schwennicke, A. Koner, J. B. Pérez-Sánchez, W. Xiong, N. C. Giebink, M. L. Weichman, and J. Yuen-Zhou, When do molecular polaritons behave like optical filters?, arXiv preprint arXiv:2408.05036 (2024).
- [52] D. Sidler, T. Schnappinger, A. Obzhairov, M. Ruggenthaler, M. Kowalewski, and A. Rubio, Unraveling a cavity-induced molecular polarization mechanism from collective vibrational strong coupling, *The Journal of Physical Chemistry Letters* **15**, 5208 (2024).
- [53] T. E. Li and S. Hammes-Schiffer, Qm/mm modeling of vibrational polariton induced energy transfer and chemical dynamics, *Journal of the American Chemical Society* **145**, 377 (2022).
- [54] W. Ahn, J. F. Triana, F. Recabal, F. Herrera, and B. S. Simpkins, Modification of ground-state chemical reactivity via light-matter coherence in infrared cavities, *Science* **380**, 1165 (2023).

- [55] E. W. Fischer and P. Saalfrank, Ground state properties and infrared spectra of anharmonic vibrational polaritons of small molecules in cavities, *The Journal of Chemical Physics* **154** (2021).
- [56] D. Jasrasaria, A. Mandal, D. R. Reichman, and T. C. Berkelbach, Simulating anharmonic vibrational polaritons beyond the long wavelength approximation, *The Journal of Chemical Physics* **162** (2025).
- [57] L. Attal, F. Calvo, C. Falvo, and P. Parneix, Coherent state switching using vibrational polaritons in an asymmetric double-well potential, *Physical Chemistry Chemical Physics* **26**, 7534 (2024).
- [58] J. Bonini and J. Flick, Ab initio linear-response approach to vibro-polaritons in the cavity born–oppenheimer approximation, *Journal of Chemical Theory and Computation* **18**, 2764 (2022).
- [59] J. Flick, H. Appel, M. Ruggenthaler, and A. Rubio, Cavity born–oppenheimer approximation for correlated electron–nuclear-photon systems, *Journal of chemical theory and computation* **13**, 1616 (2017).
- [60] P. Saurabh and S. Mukamel, Two-dimensional infrared spectroscopy of vibrational polaritons of molecules in an optical cavity, *The Journal of chemical physics* **144** (2016).
- [61] Z. Zhang, K. Wang, Z. Yi, S. Mukamel, and M. O. Scully, Local fluctuations of vibrational polaritons monitored by two-dimensional infrared spectroscopy, arXiv preprint arXiv:1806.06431 (2018).
- [62] Z. Zhang, X. Nie, D. Lei, and S. Mukamel, Multidimensional coherent spectroscopy of molecular polaritons: Langevin approach, *Physical Review Letters* **130**, 103001 (2023).
- [63] D. Gallego-Valencia, L. Mewes, J. Feist, and J. L. Sanz-Vicario, Coherent multidimensional spectroscopy in polariton systems, *Physical Review A* **109**, 063704 (2024).
- [64] J. Ren and Z. Zhang, Two-dimensional femtosecond stimulated raman spectroscopy for molecular polaritons: Dark states and beyond, *Physical Review A* **109**, 053719 (2024).
- [65] R. F. Ribeiro, A. D. Dunkelberger, B. Xiang, W. Xiong, B. S. Simpkins, J. C. Owrutsky, and J. Yuen-Zhou, Theory for nonlinear spectroscopy of vibrational polaritons, *The journal of physical chemistry letters* **9**, 3766 (2018).
- [66] Z. Zhang, K. Wang, Z. Yi, M. S. Zubairy, M. O. Scully, and S. Mukamel, Polariton-assisted cooperativity of molecules in microcavities monitored by two-dimensional infrared spectroscopy, *The journal of physical chemistry letters* **10**, 4448 (2019).
- [67] T. Schnappinger, C. Falvo, and M. Kowalewski, Disentangling collective coupling in vibrational polaritons with double quantum coherence spectroscopy, *The Journal of chemical physics* **161** (2024).
- [68] Z. Zhou, H.-T. Chen, M. Sukharev, J. E. Subotnik, and A. Nitzan, On the nature of two-photon transitions for a collection of molecules in a fabry–perot cavity, *The Journal of Chemical Physics* **160** (2024).
- [69] A. Debnath, C. Meier, B. Chatel, and T. Amand, Chirped laser excitation of quantum dot excitons coupled to a phonon bath, *Physical Review B—Condensed Matter and Materials Physics* **86**, 161304 (2012).
- [70] A. Debnath, C. Meier, B. Chatel, and T. Amand, High-fidelity biexciton generation in quantum dots by chirped laser pulses, *Physical Review B—Condensed Matter and Materials Physics* **88**, 201305 (2013).
- [71] F. P. Bonafé, E. I. Albar, S. T. Ohlmann, V. P. Kosheleva, C. M. Bustamante, F. Troisi, A. Rubio, and H. Appel, Full minimal coupling maxwell-tddft: An ab initio framework for light-matter interaction beyond the dipole approximation, *Physical Review B* **111**, 085114 (2025).
- [72] J. Flick and P. Narang, Cavity-correlated electron-nuclear dynamics from first principles, *Physical review letters* **121**, 113002 (2018).
- [73] J. Flick and P. Narang, Ab initio polaritonic potential-energy surfaces for excited-state nanophotonics and polaritonic chemistry, *The Journal of Chemical Physics* **153** (2020).
- [74] D. Sidler, M. Ruggenthaler, C. Schäfer, E. Ronca, and A. Rubio, A perspective on ab initio modeling of polaritonic chemistry: The role of non-equilibrium effects and quantum collectivity, *The Journal of Chemical Physics* **156** (2022).
- [75] M. Gruebele and P. G. Wolynes, Vibrational energy flow and chemical reactions, *Accounts of chemical research* **37**, 261 (2004).
- [76] G. D. Wiesehan and W. Xiong, Negligible rate enhancement from reported cooperative vibrational strong coupling catalysis, *The Journal of Chemical Physics* **155** (2021).
- [77] G. Engelhardt and J. Cao, Unusual dynamical properties of disordered polaritons in microcavities, *Physical Review B* **105**, 064205 (2022).
- [78] G. Engelhardt and J. Cao, Polariton localization and dispersion properties of disordered quantum emitters in multimode microcavities, *Physical review letters* **130**, 213602 (2023).
- [79] J. Cao, Generalized resonance energy transfer theory: Applications to vibrational energy flow in optical cavities, *The Journal of Physical Chemistry Letters* **13**, 10943 (2022).
- [80] F. J. Garcia-Vidal, C. Ciuti, and T. W. Ebbesen, Manipulating matter by strong coupling to vacuum fields, *Science* **373**, eabd0336 (2021).
- [81] Y. Pang, A. Thomas, K. Nagarajan, R. M. Vergauwe, K. Joseph, B. Patrahaui, K. Wang, C. Genet, and T. W. Ebbesen, On the role of symmetry in vibrational strong coupling: the case of charge-transfer complexation, *Angewandte Chemie International Edition* **59**, 10436 (2020).
- [82] A. Thomas, L. Lethuillier-Karl, K. Nagarajan, R. M. Vergauwe, J. George, T. Chervy, A. Shalabney, E. Devaux, C. Genet, J. Moran, *et al.*, Tilting a ground-state reactivity landscape by vibrational strong coupling, *Science* **363**, 615 (2019).
- [83] J. C. Wright, D. D. Kohler, and U. Bergmann, X-ray/extreme ultraviolet floquet state multidimensional spectroscopy, an analogue of multiple quantum nuclear magnetic resonance, *The journal of physical chemistry letters* **14**, 4908 (2023).
- [84] B. Patrahaui, M. Piejko, R. J. Mayer, C. Antheaume, T. Sangchai, G. Ragazzon, A. Jayachandran, E. Devaux, C. Genet, J. Moran, *et al.*, Direct observation of polaritonic chemistry by nuclear magnetic resonance spectroscopy, *Angewandte Chemie International Edition* **63**, e202401368 (2024).

- [85] M. Gruebele, The fast protein folding problem, *Annual review of physical chemistry* **50**, 485 (1999).
- [86] F. Moradi Kalarde, F. Ciccarello, C. Sánchez Muñoz, J. Feist, and C. Galland, Photon antibunching in single-molecule vibrational sum-frequency generation, *Nanophotonics* **14**, 59 (2025).
- [87] V. Vento, P. Roelli, S. Verlekar, and C. Galland, Mode-specific coupling of nanoparticle-on-mirror cavities with cylindrical vector beams, *Nano Letters* **23**, 4885 (2023).
- [88] V. Vento, S. Tarrago Velez, A. Pogrebna, and C. Galland, Measurement-induced collective vibrational quantum coherence under spontaneous raman scattering in a liquid, *Nature Communications* **14**, 2818 (2023).
- [89] J. Klafter and J. Jortner, Two-particle vibrational excitations in molecular crystals, *The Journal of Chemical Physics* **77**, 2816 (1982).
- [90] O. Christiansen, A second quantization formulation of multimode dynamics, *The Journal of chemical physics* **120**, 2140 (2004).
- [91] O. Christiansen, Vibrational coupled cluster theory, *The Journal of chemical physics* **120**, 2149 (2004).